RESEARCH ARTICLE | OPEN ACCESS

Convergence of Damped Polarization Schemes for the FFT-Based Computational Homogenization of Inelastic Media With Pores

Elodie Donval[1] [iD] | Matti Schneider[1,2] [iD]

[1]Institute of Engineering Mathematics, University of Duisburg-Essen, Essen, Germany | [2]Department of Flow and Material Simulation, Fraunhofer Institute for Industrial Mathematics ITWM, Kaiserslautern, Germany

Correspondence: Matti Schneider (matti.schneider@uni-due.de)

ABSTRACT

Porous microstructures represent a challenge for the convergence of FFT-based computational homogenization methods. In this contribution, we show that the damped Eyre–Milton iteration is linearly convergent for a class of nonlinear composites with a regular set of pores, provided the damping factor is chosen between zero and unity. First, we show that an abstract fixed-point method with non-expansive fixed-point operator and non-trivial damping converges linearly, provided the associated residual mapping satisfies a monotonicity condition on a closed subspace. Then, we transfer this result to the framework of polarization schemes and conclude the linear convergence of the damped Eyre–Milton scheme for porous materials. We present general arguments which apply to a class of nonlinear composites and mixed stress-strain loadings, as well. We show that the best contraction estimate is reached for a damping factor of 1/2, that is, for the polarization scheme of Michel–Moulinec–Suquet, and derive the corresponding optimal reference material. Our results generalize the recent work of Sab and co-workers who showed that an adaptively damped Eyre–Milton scheme leads to linear convergence for a class of linear composites with pores. Finally, we report on computational experiments which support our findings.

1 | Introduction

FFT-based homogenization methods were introduced by Moulinec and Suquet at the end of the 1990s [1, 2]. They quickly became a popular tool for computational micromechanics thanks to their multiple advantages. Indeed, they allow for direct computation on 2D or 3D images, which may be obtained by a CT scan for instance. Their matrix-free nature makes them memory efficient and hence adapted to industrial problems. Moreover, over the last 30 years, a lot of work was invested [3–5]

to improve the capabilities of these techniques, focusing mainly on two core aspects: discretization techniques and solvers.

Several different discretizations have been introduced since then, aiming at reducing the ringing artifacts characteristic of the initial Moulinec–Suquet discretization, which is based on trigonometric polynomials. For instance, the rotated staggered grid discretization [6] reduces the spurious oscillations characteristic for trigonometric polynomials at the expense of introducing a checkerboard pattern. The staggered grid discretization [7]

avoids those checkerboard patterns, but the position of the integration points may complicate the handling of anisotropic materials. Closely related to the two previously cited finite-difference discretizations, some finite-element [8, 9] and finite-volume discretizations [10, 11] were also introduced. Fully integrated Fourier-Galerkin discretizations [12–14] allow to derive bounds on the macroscopic stiffness but are limited to linear elastic materials. Finally, some other discretizations, based on the Hashin-Shtrikman principle [15, 16], B-splines [17], interpolative wavelets [18] or the Radon transform [19] were considered.

Concerning solvers, Moulinec and Suquet's basic scheme represents a purely primal approach, operating only on the strain field. It may be interpreted as a gradient descent method to minimize the free energy [20]. Building on this aspect, several improvements were proposed, such as an adaptive step-size based on the Barzilai-Borwein rule [21, 22], fast-gradient methods [23, 24], or Anderson acceleration [25, 26]. Other strategies, such as the linear and nonlinear conjugate gradient method [15, 27, 28], Newton-type methods [20, 29, 30] and Quasi-Newton schemes [31], were also considered. As noticed by Milton [32], §14 and Bhattacharya–Suquet [33], the basic scheme may also be developed in a dual framework, that is, based on the stresses rather than on the strains, and take advantage of most of the improvements proposed for the primal basic scheme. Dual solvers are of practical interest for some specific constitutive laws [34] where they are less computationally expensive than primal solvers.

Aside from primal and dual approaches, polarization approaches quickly emerged, which operate on a local polarization field that is neither compatible nor equilibrated. They were first introduced in the linear setting for conductivity problems, by Eyre and Milton [35]. Then, Michel et al. [36, 37] transferred polarization approaches to the framework of inelastic solid mechanics. A more general class of polarization schemes was proposed by Monchiet and Bonnet, first in the linear setting [38], then in a nonlinear one [39]. Moulinec and Silva [40] later showed that all polarization schemes could be united under a common formulation for linear constitutive laws. Schneider et al. [41] extended this unified formulation to the nonlinear setting and connected the Eyre–Milton scheme to an existing numerical technique, the Peaceman-Rachford splitting [42], and its damped variant to the Douglas-Rachford splitting [43]. By taking advantage of convergence results for the two splitting techniques [44], they identified optimal algorithmic parameters in the case of finite material contrast. These results do not cover the case of infinite material contrast, for example, in the presence of pores. Then, resorting to adaptive algorithmic parameters can prove useful [45, 46] and bring the efficiency of polarization approaches to the level of primal schemes.

The porous, infinitely-contrasted case also challenges the choice of algorithmic parameters, and the existence of linearly convergent polarization schemes has been questioned for a long time [41]. For primal solvers, different authors [7, 47] noticed that the lack of convergence was caused by the discretization rather than by the solver. This insight was put on a firm mathematical basis by Schneider [48], who proved that the continuous, non-discretized basic scheme converges linearly on a class of porous microstructures. In particular, the convergence of the solver depends not only on the material contrast as for non-porous microstructures, but also on the geometry of the interface. However, not all discretizations preserve this linear convergence property. In fact, linear convergence is preserved by some finite difference [6, 7] discretizations, while spectral discretizations such as the initial one proposed by Moulinec and Suquet [1, 2] and Fourier-Galerkin discretizations [12–14] usually lead to numerical instabilities. While a linear convergence result exists for primal solvers, the question of the linear convergence of polarization approaches remained open. The recent publication from Sab et al. [49] provided some answers by exhibiting a linear convergent, Eyre–Milton-like solver for a class of microstructures containing both pores and rigid inclusions. The proposed scheme selects the damping factor adaptively based on a suitable online eigenvalue estimate. However, both the scheme and its analysis are intrinsically restricted to linear constitutive laws.

In the present contribution, we show the linear convergence of the damped Eyre–Milton (DEM) scheme with a fixed non-trivial damping factor on a rather general class of porous microstructures.

The article at hand comprises both a theoretical and a computational part. We provide a short overview of the theoretical arguments in Section 2 to increase the readability of this work. Sections 3 and 4 contain the more detailed arguments. More precisely, in Section 3, we consider degenerate fixed-point methods in an abstract setting. It is well-known [50] that a contractive mapping on a Banach space possesses a unique fixed point, and the associated fixed-point scheme converges globally and linearly to this fixed point. In the case of a merely non-expansive mapping, matters are more complicated. The celebrated Krasnoselskii-Mann Theorem, see Ryu–Yin [51], § 2.4, Theorem 1 for a proof, states that for a non-expansive mapping on a Banach space which has a fixed point, the damped fixed-point iteration with non-trivial damping converges weakly to the fixed-point set with a sublinear, that is, logarithmic rate. In the work at hand, we work out a non-degeneracy condition of the residual mapping on a closed subspace, which renders the associated damped fixed-point scheme linearly convergent to the unique fixed point within the subspace. These results are of independent interest, in particular, as the level of abstraction permits the presentation of the arguments in a classroom setting, for instance.

Then, Section 4 is devoted to transferring the linear convergence result obtained in Section 3 to the context of polarization schemes. More precisely, we derive a linear convergence estimate in a general framework, including mixed stress-strain loadings and nonlinear material behavior. We start by defining the fixed-point mapping encoding the Eyre–Milton scheme. For microstructures with finite contrast, this mapping is a contraction mapping [41] and ensures the linear convergence of the Eyre–Milton scheme. In the case of porous microstructures, however, this mapping is only non-expansive. We show that the residual mapping associated with the Eyre–Milton scheme complies with the conditions established in Section 3. By resorting to the convergence result established in the latter section, we show that linear convergence of the damped scheme is ensured for any fixed damping factor in the open interval $(0, 1)$. A theoretical bound on the convergence speed of the damped Eyre–Milton scheme is obtained through the convergence analysis, and the values

of reference material and damping that optimize the theoretical bound are derived. Finally, in Section 5, we present several computational experiments to support our theoretical findings.

2 | An Outline of the Arguments

2.1 | The Point of Departure

It is by now well-known in the community that primal Lippmann-Schwinger solvers also converge in the presence of pores, provided the solid material distribution and the constitutive laws lead to a mechanically stable microstructure and a proper discretization is used, for example, the staggered grid [7], finite elements [8, 9, 52] or the tetrahedral discretization scheme [53]. The theoretical analysis [48] reveals that the reason for this convergence lies in a coercivity estimate which permits to bound of the total "energy" on the entire cell by the "energy" in the solid skeleton. Of course, such a property cannot hold for a general strain field, because one may select a strain field which is non-zero in the pore space but vanishes in the solid skeleton. However, it is readily observed that the original basic scheme and its direct derivatives preserve strains that are compatible and satisfy the balance of linear momentum in the pore space w.r.t. the elastic properties inscribed into the pore space by the reference material $\mathbb{C}^0$. Thus, if the initial strain is compatible and $\mathbb{C}^0$-balanced in the pore space, all subsequent iterates will be compatible and $\mathbb{C}^0$-balanced in the pore space, as well. Moreover, the elastic energy within the pore space is fully determined by the displacement boundary conditions on the interface between the pore and solid material. Thus, up to mathematical details, this transfer mechanism is responsible for the fact that the elastic energy within pore space is controlled by the energy in the solid skeleton.

A direct translation of this analysis to polarization schemes [35, 37] is not straightforward, as they operate on the stress polarization

$$P = \sigma + \mathbb{C}^0 : \varepsilon \qquad (1)$$

instead of the strain field, where we may assume an elastic behavior $\sigma = \mathbb{C} : \varepsilon$ for the discussion presented in this section. Also, polarization schemes have a very different character than the classical primal solvers. Whereas the primal solvers are easily understood as modifications and extensions of the classical *gradient-descent method*, the analysis of polarization schemes is based on the contraction-mapping theorem, that is, that any endomorphism $F : X \to X$ of a Banach space X with a Lipschitz constant strictly less than unity possesses a unique fixed point x^* and the classical fixed-point scheme

$$x^{k+1} = F(x^k) \qquad (2)$$

converges linearly to the fixed point x^*.

In the presence of pores, the fixed-point operator F associated with the Eyre–Milton method is not a contraction. Rather, its Lipschitz constant is unity. Such a piece of information is not sufficient per se, in general, as there are operators without fixed points, for example, translations in Euclidean space.

In the seminal work [49], Sab et al. proposed to consider the relaxed iterative scheme

$$x^{k+1} = \gamma_k \, x^k + (1 - \gamma_k) \, F(x^k) \qquad (3)$$

with an adaptive damping factor $\gamma_k > 0$. They showed that, in the context of linear elasticity and stable pore space, the iterative scheme (3) is linearly convergent on a suitable subspace and provided the damping factor γ_k is selected via an associated optimization problem. The subspace consists of those polarizations (1) which are equilibrated in the pore space.

Despite the breakthrough character of the work [49], there are several shortcomings. For a start, the scheme (3) does not cover the classical, that is, non-adaptive methods. Secondly, the scheme (3) and its analysis both rely on a linear constitutive law, ruling out inelastic micromechanics with significant practical and industrial interest. Last but not least, the simplicity of the original approach to Eyre–Milton schemes [35, 41], that is, a direct application of the contraction-mapping theorem, is lost.

2.2 | Abstracting and Generalizing the Original Proof

We sought a generalization of the classical contraction mapping theorem which permits us to analyze some degenerate cases, as well. To illustrate the point, suppose that we have a contraction mapping $F : X \to X$ on a Banach space X with contraction constant $c_- \in (0, 1)$. Let us artificially cook up a degenerate case by considering the mapping

$$\tilde{F} : X \oplus X \to X \oplus X, \quad \tilde{F}\left(\begin{bmatrix} x \\ y \end{bmatrix}\right) = \begin{bmatrix} F(x) \\ y \end{bmatrix} \qquad (4)$$

Thus, we consider tuples of inputs and apply the contraction mapping F to the first input but do not change the second input. The mapping $\tilde{F}$ has the Lipschitz constant 1, so the contraction mapping theorem does not apply. However, we directly observe that there is, in fact, a unique fixed point, and the naturally associated fixed-point scheme converges linearly to this unique fixed point. In fact, it is just the fixed point scheme associated with the original mapping F in disguise.

To be able to treat this situation, it is helpful to consider the (vector) residual

$$R : X \to X, \quad R(x) = x - F(x) \qquad (5)$$

The roots of the residual coincide with the fixed points of the mapping F. The residual associated to the lifted mapping (4) reads

$$\tilde{R}\left(\begin{bmatrix} x \\ y \end{bmatrix}\right) = \begin{bmatrix} x - F(x) \\ 0 \end{bmatrix} \qquad (6)$$

and we may infer convergence statements for this type of formulation.

This motivational example is not general enough for our problem, essentially because the example does not feature a coupling

between the two inputs. A key insight of Sab et al. [49] is the estimate

$$(x - y, R(x) - R(y)) \geq c \, \|x - y\|^2 \qquad (7)$$

valid for the Eyre–Milton operator and polarization fields x and y in the subspace discussed in the previous section. Here, we consider a suitably weighted L^2-Hilbert space of polarization fields and the constant c is positive and independent of the fields x and y.

From a mathematical perspective, the estimate (7) encodes the fact that the residual operator R is a strongly monotone operator on the subspace. In particular, there is a unique root of the residual.

In this work, we use the estimate (7) as a starting point and show that, provided the fixed-point mapping F has the Lipschitz constant 1, the damped fixed-point mapping

$$x^{k+1} = \gamma \, x^k + (1 - \gamma) F(x^k) \qquad (8)$$

is linearly convergent for any starting point x^0 in the subspace and any fixed damping factor $\gamma \in (0, 1)$. In particular, these results imply that the adaptivity in the damping parameter proposed by Sab et al. [49] is not strictly necessary for the linear convergence of the damped Eyre–Milton scheme in the presence of pores. We present the corresponding arguments in Section 3.

We wish to highlight that the results we obtain are stronger than those obtained by Sab et al. [49], even for linear elasticity. The results of the paper [49] lead to the conclusion that the damped fixed-point mapping (8) converges for a damping factor $\gamma \in (0, \gamma^+)$ inside an open interval, where $\gamma^+ > 0$ is a potentially small number. With the help of a more careful estimate, we show that γ^+ can be chosen as one.

2.3 | Key Arguments in the Linear Case

We identified the coercivity estimate (7) as the key ingredient to the successful analysis of the damped Eyre–Milton scheme in the presence of pores. Let us briefly discuss how this estimate is established in the case of linear elasticity. For this purpose, we introduce the Eyre–Milton fixed-point operator

$$F(P) = 2 \, \mathbb{C}^0 : \bar{\varepsilon} + \mathbb{Y}^0 : \mathbb{Z}^0 : P \qquad (9)$$

with the reflection operator

$$\mathbb{Y}^0 = \mathrm{Id} - 2 \, \mathbb{C}^0 : \Gamma^0 \qquad (10)$$

and the "constitutive law"-enforcing operator

$$\mathbb{Z}^0 = (\mathbb{C} - \mathbb{C}^0) : (\mathbb{C} + \mathbb{C}^0)^{-1} \qquad (11)$$

where $\mathbb{C}$ denotes the local stiffness field, $\mathbb{C}^0$ refers to the reference stiffness and Γ^0 stands for the associated Eshelby-Green operator. The operator (11) splits a given polarization P into the associated stress σ and strain ε via

$$\sigma = \mathbb{C} : (\mathbb{C} + \mathbb{C}^0)^{-1} : P \quad \text{as well as} \quad \varepsilon = (\mathbb{C} + \mathbb{C}^0)^{-1} : P \quad (12)$$

and changes their "polarization"

$$\mathbb{Z}^0 : P = \sigma - \mathbb{C}^0 : \varepsilon \qquad (13)$$

In a sense, the operator $\mathbb{Z}^0$ is also a "reflection operator", keeping the stress and (additively) inverting the strain. For two polarization fields split according to Equation (12), the difference of residuals takes the form

$$R(P_1) - R(P_2)$$
$$= 2\mathbb{C}^0 : \Gamma^0 : (\sigma_1 - \sigma_2) + 2\mathbb{C}^0 : (\mathrm{Id} - \Gamma^0 : \mathbb{C}^0) : (\varepsilon_1 - \varepsilon_2) \qquad (14)$$

At this point, we assume the reference material to be proportional to the identity to simplify some expressions with $\Gamma \equiv \Gamma^0 : \mathbb{C}^0$. With an eye towards the desired estimate (7), one tests this field with the difference $P_1 - P_2$ to obtain

$$\frac{1}{2}\big(R(P_1) - R(P_2), P_1 - P_2\big)$$
$$= \big(\Gamma : (\sigma_1 - \sigma_2), P_1 - P_2\big) \qquad (15)$$
$$+ \big(\mathbb{C}^0 : (\mathrm{Id} - \Gamma) : (\varepsilon_1 - \varepsilon_2), P_1 - P_2\big)$$

Here, the symbol $(\cdot, \cdot)$ denotes the L^2-inner product of fields on the considered cell. Let us rewrite the splitting (12) in operator form with operators

$$\mathbb{J}^0 = \mathbb{C} : (\mathbb{C} + \mathbb{C}^0)^{-1} \quad \text{and} \quad \mathbb{K}^0 = \mathbb{C}^0 : (\mathbb{C} + \mathbb{C}^0)^{-1} \qquad (16)$$

These operators are complementary in the sense that their sum is just the identity. Moreover, they permit to express the splitting (12) via

$$\sigma = \mathbb{J}^0 : P \quad \text{and} \quad \mathbb{C}^0 : \varepsilon = \mathbb{K}^0 : P \qquad (17)$$

In particular, we may recast the identity (15) in the form

$$\frac{1}{2}\big(R(P_1) - R(P_2), P_1 - P_2\big)$$
$$= \big(\Gamma : \mathbb{J}^0 : (P_1 - P_2), P_1 - P_2\big) \qquad (18)$$
$$+ \big((\mathrm{Id} - \Gamma) : \mathbb{K}^0 : (P_1 - P_2), P_1 - P_2\big)$$

At this point, we note that the operators Γ and $(\mathrm{Id} - \Gamma)$ project onto compatible and equilibrated fields, but they do not act on the stress polarizations P_i ($i = 1, 2$) directly. A critical observation of Sab et al. [49] is the equivalent form

$$\frac{1}{2}\big(R(P_1) - R(P_2), P_1 - P_2\big)$$
$$= \big(\mathbb{J}^0 : \Gamma : (P_1 - P_2), \Gamma : (P_1 - P_2)\big) \qquad (19)$$
$$+ \big(\mathbb{K}^0 : (\mathrm{Id} - \Gamma) : (P_1 - P_2), (\mathrm{Id} - \Gamma) : (P_1 - P_2)\big)$$

of the identity (18), which is based on ingenious algebraic manipulations using the complementarity of the orthogonal operators Γ and $(\mathrm{Id} - \Gamma)$ and the symmetry/complementarity of the operators (17).

To arrive at the desired estimate (7), one may argue as follows. The second summand (19) involves the operator $\mathbb{K}^0$ which is non-zero everywhere and whose eigenvalues are bounded from below away from zero. Thus, we get an L^2-bound on the part $(\mathrm{Id} - \Gamma) : (P_1 - P_2)$. The first summand in Equation (19) is more subtle, because the operator $\mathbb{J}^0$ vanishes in the pore space. However, the field $\Gamma : (P_1 - P_2)$ is compatible, and we may recover an estimate for the pore-space contribution from the subspace property, just like for primal solvers.

2.4 | Extension to Nonlinear Problems

The key steps described in Section 2.3 are intrinsically linear, and do not readily generalize to the inelastic/nonlinear setting. A reasonable class of nonlinear constitutive laws was identified by Schneider et al. [41] to comprise gradients of strongly convex functions which moreover satisfy a Lipschitz condition. Once this class of constitutive laws is fixed, a well-defined extension of the Eyre–Milton scheme (9) is straightforward, at least from a theoretical point of view. More precisely, the linear operator $\mathbb{Z}^0$ needs to be replaced by a suitable nonlinear operator $\boldsymbol{Z}^0$, and the same is true for the two operators $\mathbb{J}^0$ and $\mathbb{K}^0$. Due to the assumed monotonicity of the stress mapping, the required inversions make sense and the (generalized) operators $\boldsymbol{Z}^0$, $\boldsymbol{J}^0$ and $\boldsymbol{K}^0$ are well-defined. By a similar argument as before, one arrives at the representation

$$\frac{1}{2}\big(\boldsymbol{R}(\boldsymbol{P}_1) - \boldsymbol{R}(\boldsymbol{P}_2), \boldsymbol{P}_1 - \boldsymbol{P}_2\big)$$
$$= \big(\boldsymbol{\Gamma} : (\boldsymbol{J}^0(\boldsymbol{P}_1) - \boldsymbol{J}^0(\boldsymbol{P}_2)), \boldsymbol{P}_1 - \boldsymbol{P}_2\big) \qquad (20)$$
$$+ \big((\mathrm{Id} - \boldsymbol{\Gamma}) : (\boldsymbol{K}^0(\boldsymbol{P}_1) - \boldsymbol{K}^0(\boldsymbol{P}_2)), \boldsymbol{P}_1 - \boldsymbol{P}_2\big)$$

However, a simple swapping of the nonlocal operators and the local operators $\boldsymbol{J}^0/\boldsymbol{K}^0$ is not directly possible due to the nonlinearity. To proceed, we use the Fundamental Theorem of Calculus to rewrite, for instance, the term

$$\boldsymbol{J}^0(\boldsymbol{P}_1) - \boldsymbol{J}^0(\boldsymbol{P}_2) = \int_0^1 \frac{\partial \boldsymbol{J}^0}{\partial \boldsymbol{P}}(\boldsymbol{P}_2 + s(\boldsymbol{P}_1 - \boldsymbol{P}_2)) : [\boldsymbol{P}_1 - \boldsymbol{P}_2]\, ds \qquad (21)$$

as a superposition of linear operators. Pulling the integral out of all terms, we end up with an averaged version of the estimate (18) involving linear operators only. As the gradients of strongly monotone operators are (linear) strongly monotone operators with the same monotonicity constant, the linear arguments actually extend to this kind of nonlinear case. Please note that the argument depends on the differentiability of the stress mapping. However, the case of a non-differentiable stress mapping may be dealt with via an approximation argument. Alternatively, Rademacher's theorem [54] ensures that the stress mapping is differentiable almost everywhere, which would also legitimate the discussion.

The sketched argument extends the convergence results for the damped Eyre–Milton scheme to porous materials whose constitutive laws inside the solid skeleton are monotone and Lipschitz. We refer to Section 4 for details.

2.5 | Dealing With Mixed Boundary Conditions

There is a last small issue, which is relevant to the nonlinear/inelastic setting. For linear elasticity, the apparent stiffness of the microstructure is sought. Therefore, it is convenient to determine the effective stiffness matrix column-wise by prescribing the macroscopic strain and computing the effective stress afterward. Specific experimental setups may be reproduced in postprocessing, for example, extracting the directional Young's moduli from the compliance matrix. For the inelastic setting, such an intrinsically linear procedure does not readily apply. Rather, mixed boundary conditions [55] need to be imposed and accounted for

in the scheme. For polarization schemes in Eyre–Milton form, the relevant procedure is described in Schneider et al. [41].

Returning to the setting of pores, it turns out that the arguments for prescribed strain are not sufficient to handle the case of mixed boundary conditions. Rather, the projectors $\boldsymbol{\Gamma}$ and $(\mathrm{Id} - \boldsymbol{\Gamma})$ need to be modified, and a more refined subspace-argument is required. The details comprise Appendix A3.

3 | Linear Convergence Theory for Degenerate Fixed-Point Methods

The theoretical underpinnings of the considered degenerate fixed-point method(s) are best explained in a suitable abstract framework. Dealing with several different cases at once is not our goal, here. Rather, we would like to work out the different mathematical mechanisms at play, fostering the understanding of the inner workings.

We consider a Hilbert space H, together with a non-expansive mapping $F : H \to H$, that is, which satisfies the non-expansivity estimate

$$\|F(x) - F(y)\| \leq \|x - y\| \quad \text{for all} \quad x, y \in H \qquad (22)$$

The associated fixed-point method

$$x^{k+1} = F(x^k), \quad k = 0, 1, \dots \qquad (23)$$

for some starting point $x^0 \in H$ is not necessarily convergent–consider, for example, the case where the mapping F corresponds to the shift by a non-zero vector–and there is no fixed point, or where the mapping F is an orthogonal transformation. The latter example can be made convergent by considering the damped fixed-point method

$$x^{k+1} = F_\gamma(x^k), \quad k = 0, 1, \dots \qquad (24)$$

with the damped fixed-point operator

$$F_\gamma : H \to H, \quad x \mapsto \gamma x + (1 - \gamma) F(x), \quad \gamma \in [0, 1) \qquad (25)$$

The original mapping F is recovered in the special case $F_0 \equiv F$.

Under rather minimal assumptions, that is, the mapping F is non-expansive (22) and the fixed-point set of the mapping F is non-empty, the damped fixed-point method (24) for fixed damping $\gamma \in (0, 1)$ can be shown to be weakly convergent, and the distance to the fixed-point set decreases with a logarithmic rate, see Ryu-Yin [51], § 2.4, Theorem 1. For the setup at hand, we consider more restrictive assumptions and show that the scheme (24) converges strongly and with a linear rate for any damping $\gamma \in (0, 1)$.

Any fixed point x^* of the iterative scheme (25) is a root of the residual mapping

$$R : H \to H, \quad R(x) = x - F(x) \qquad (26)$$

that is, the equation

$$R(x^*) = 0 \qquad (27)$$

holds. We consider a closed subspace $H_0 \subseteq H$ which is stable under the action of the residual mapping (26), that is, it satisfies

$$R(x_0) \in H_0 \quad \text{for all} \quad x_0 \in H_0. \tag{28}$$

As a consequence, the representation

$$F_\gamma(x) = \gamma \, x + (1 - \gamma) \, F(x) = x - (1 - \gamma) \, R(x) \tag{29}$$

reveals that the damped fixed-point operator (25) preserves the space H_0.

We work under the following assumption:

- There is a constant c_-, s.t. the strong monotonicity estimate

$$c_- \, \|x - y\|^2 \le (x - y, R(x) - R(y)), \quad x, y \in H_0 \tag{30}$$

  holds on the closed subset H_0 satisfying Equation (28). Here, the round brackets refer to the inner product on the Hilbert space H.

Under this assumption, we establish the following consequences:

1. There is a unique root x^* of the residual mapping (27) on the space H_0.

2. For any starting point $x^0 \in H^0$ and any damping parameter $\gamma \in (0, 1)$, the associated damped fixed-point scheme (24) is *linearly* convergent, see Equation (35) below for the exact estimate.

3. The bound on the contraction factor of the mapping F_γ on the space H_0 is minimized for the choice $\gamma = 1/2$ with contraction constant $\sqrt{1 - c_-/2}$.

To establish these claims, we need another bound to complement the monotonicity estimate (30). More precisely, the residual mapping R is 2-co-coercive on the space H, that is, the estimate

$$\frac{1}{2} \|R(x) - R(y)\|^2 \le (x - y, R(x) - R(y)), \quad x, y \in H \tag{31}$$

holds. Before establishing the validity of this estimate, let us briefly comment that co-coercivity is stronger than Lipschitz continuity. In fact, combining the estimate (31) with the Cauchy-Schwarz inequality yields the chain of arguments

$$\|R(x) - R(y)\|^2 \le 2 \, (x - y, R(x) - R(y))$$
$$\le 2 \, \|x - y\| \, \|R(x) - R(y)\| \tag{32}$$

that is, the Lipschitz continuity (with Lipschitz constant 2) of the residual mapping (26).

To establish the estimate (31), we recall the definition of the residual mapping (26) in terms of the fixed-point mapping F and use the binomial formula

$$\|R(x) - R(y)\|^2$$
$$= \|x - y - [F(x) - F(y)]\|^2 \tag{33}$$
$$= \|x - y\|^2 - 2 \, (x - y, F(x) - F(y)) + \|F(x) - F(y)\|^2$$

By the assumed non-expansivity (22) of the mapping F, we are thus led to the estimate

$$\|R(x) - R(y)\|^2$$
$$= \|x - y\|^2 - 2 \, (x - y, F(x) - F(y)) + \|F(x) - F(y)\|^2$$
$$\le \|x - y\|^2 - 2 \, (x - y, F(x) - F(y)) + \|x - y\|^2$$
$$= 2\big(\|x - y\|^2 - (x - y, F(x) - F(y))\big) \tag{34}$$
$$= 2(x - y, x - y - [F(x) - F(y)])$$
$$= 2(x - y, R(x) - R(y))$$

Thus, the desired co-coercivity estimate (31) is established.

With these prerequisites at hand, standard fixed-point arguments [51], §2.4.3 permit us to derive the estimate

$$\left\| F_\gamma(x) - F_\gamma(y) \right\| \le \sqrt{1 - 2c_- \, \gamma(1 - \gamma)} \, \|x - y\|, \quad x, y \in H_0 \tag{35}$$

for damping $\gamma \in (0, 1)$, which implies all three claims. In fact, Banach's fixed point theorem [51], §2.4.2 yields the existence of a unique fixed point $x^* \in H_0$, which establishes property 1. The contraction estimate (35) leads to the validity of property 2. Last but not least, it is easily seen that the quadratic function

$$\rho(\gamma) = 1 - 2c_- \, \gamma(1 - \gamma) \tag{36}$$

is minimized for $\gamma = 1/2$ with value

$$\rho\left(\frac{1}{2}\right) = 1 - \frac{c_-}{2} \tag{37}$$

Thus, it remains to establish the estimate (35). Writing $\lambda = 1 - \gamma$ in the expression (29), we use the binomial formula to expand the difference

$$\left\| F_\gamma(x) - F_\gamma(y) \right\|^2$$
$$= \|x - y - \lambda \, [R(x) - R(y)]\|^2$$
$$= \|x - y\|^2 - 2\lambda(x - y, R(x) - R(y)) + \lambda^2 \, \|R(x) - R(y)\|^2 \tag{38}$$

The co-coercivity estimate (31) implies

$$\left\| F_\gamma(x) - F_\gamma(y) \right\|^2$$
$$= \|x - y\|^2 - 2\lambda(x - y, R(x) - R(y)) + \lambda^2 \, \|R(x) - R(y)\|^2$$
$$\le \|x - y\|^2 - 2\lambda(x - y, R(x) - R(y))$$
$$\quad + 2\lambda^2 \, (x - y, R(x) - R(y))$$
$$= \|x - y\|^2 - 2(\lambda - \lambda^2)(x - y, R(x) - R(y)) \tag{39}$$

As the term $\lambda - \lambda^2 = (1 - \lambda)\lambda = \gamma(1 - \gamma)$ is positive for any choice $\gamma \in (0, 1)$, we may use the monotonicity estimate (30) to deduce the bound

$$\left\| F_\gamma(x) - F_\gamma(y) \right\|^2$$
$$\le \|x - y\|^2 - 2 \, \gamma(1 - \gamma)(x - y, R(x) - R(y))$$
$$\le \|x - y\|^2 - 2 \, \gamma(1 - \gamma)c_-\|x - y\|^2 \tag{40}$$
$$= \big(1 - 2c_- \, \gamma(1 - \gamma)\big)\|x - y\|^2$$

which is nothing but the desired contraction estimate (35).

We close this section with a remark. The obtained results are stronger than the ones obtained in Sab et al. [49]. In fact, Sab et al. use the Lipschitz estimate

$$\| R(x) - R(y) \| \leq 2 \| x - y \|, \quad x, y \in H \tag{41}$$

to bound Equation (38) in the form

$$\begin{aligned}
\left\| F_\gamma(x) - F_\gamma(y) \right\|^2 \\
&= \| x - y \|^2 - 2\lambda(x - y, R(x) - R(y)) + \lambda^2 \| R(x) - R(y) \|^2 \\
&\leq \| x - y \|^2 - 2c_\_ \lambda \| x - y \|^2 + 4\lambda^2 \| x - y \|^2 \\
&= \left(1 - 2\,c_\_\lambda + 4\lambda^2 \right) \| x - y \|^2
\end{aligned} \tag{42}$$

The prefactor is less than unity precisely if the condition

$$\lambda < \frac{c_\_}{2} \tag{43}$$

holds, which depends on the (typically unknown) monotonicity constant $c_\_$ and is more restrictive than the choice $\lambda \in (0, 1)$ established in this section. Moreover, optimizing the constant in the estimate (42) gives the contraction factor

$$1 - 2\,c_\_\lambda + 4\lambda^2 = 1 - \frac{c_\_^2}{4} \quad \text{for} \quad \lambda = \frac{c_\_}{4} \tag{44}$$

This contraction constant is significantly worse than the one (37) established in the work at hand.

4 | The Damped Eyre–Milton Method

4.1 | The Eyre–Milton View on the Micromechanical Problem

We work on a rectangular cell

$$Y = [0, L_1] \times [0, L_2] \times \cdots \times [0, L_d] \tag{45}$$

in d dimensions, which we consider as a periodic unit cell, and an open subset $Y_p \subseteq Y$ of "pores" with Lipschitz boundary that satisfies the following regularity requirement:

$$\begin{aligned}
&\text{If a field } u \in H^1_{\mathrm{per}}(Y)^d \text{ has a homogeneous strain} \\
&\nabla^s u(x) = \text{const on } Y \setminus Y_p, \text{it is constant on } Y \setminus Y_p
\end{aligned} \tag{46}$$

This condition restricts the pore shape, ruling out mechanically unstable solid-phase configurations. It is also central to the analysis, and generalizes the assumption [48, §2.2], which only considered *vanishing strain*, to the case of mixed stress-strain loadings. We remark that the tautological case $Y_p = \emptyset$, that is, without any pore space, is included, as well.

We suppose that a free energy function

$$w : Y \times \mathrm{Sym}(d) \to \mathbb{R} \tag{47}$$

is given where $\mathrm{Sym}(d)$ denotes the vector space of symmetric $d \times d$-tensors, possibly arising as a condensation of a time-discretized variational principle [56, 57], which satisfies the following properties:

1. The energy (47) is measurable in the first variable.

2. The energy (47) vanishes on the pore space Y_p, that is,

$$w(x, \varepsilon) = 0, \quad x \in Y_p, \quad \varepsilon \in \mathrm{Sym}(d) \tag{48}$$

3. For (almost) every $x \in Y$, the energy w is continuously differentiable in the second variable and the associated stress operator [48, §2.1]

$$\begin{aligned}
S &: Y \times \mathrm{Sym}(d) \to \mathrm{Sym}(d) \\
S(x, \varepsilon) &= \frac{\partial w}{\partial \varepsilon}(x, \varepsilon), \quad x \in Y, \quad \varepsilon \in \mathrm{Sym}(d)
\end{aligned} \tag{49}$$

is $\alpha_\_$-strongly monotone in the skeleton

$$\begin{aligned}
&\left(S(x, \varepsilon_1) - S(x, \varepsilon_2), \varepsilon_1 - \varepsilon_2 \right) \\
&\geq \alpha_\_ \| \varepsilon_1 - \varepsilon_2 \|^2, \quad x \in Y \setminus Y_p, \quad \varepsilon_1, \varepsilon_2 \in \mathrm{Sym}(d)
\end{aligned} \tag{50}$$

where we use the Frobenius inner product, and α_+-Lipschitz continuous

$$\begin{aligned}
&\| S(x, \varepsilon_1) - S(x, \varepsilon_2) \| \\
&\leq \alpha_+ \| \varepsilon_1 - \varepsilon_2 \|, \quad x \in Y \setminus Y_p, \quad \varepsilon_1, \varepsilon_2 \in \mathrm{Sym}(d)
\end{aligned} \tag{51}$$

for positive constants $\alpha_\_$ and α_+.

Notice that due to the condition (48) in the pore space, the stress operator is zero:

$$S(x, \varepsilon) = 0 \quad \text{for (almost) all} \quad x \in Y_p, \quad \varepsilon \in \mathrm{Sym}(d) \tag{52}$$

Last but not least, we assume that two complementary orthogonal projectors $\mathbb{P}$ and $\mathbb{Q}$ on the space $\mathrm{Sym}(d)$ are given-where the orthogonality refers to the Frobenius inner product–together with a homogeneous strain $\overline{\varepsilon} \in \mathrm{Sym}(d)$ and a homogeneous stress $\overline{\sigma} \in \mathrm{Sym}(d)$ which satisfy the compatibility conditions

$$\mathbb{P} : \overline{\varepsilon} = \overline{\varepsilon} \quad \text{and} \quad \mathbb{Q} : \overline{\sigma} = \overline{\sigma} \tag{53}$$

We refer to Kabel et al. [55] for background, examples, and a discussion.

The problem which we want to solve [48, §2] seeks both a strain field $\varepsilon \in L^2(Y; \mathrm{Sym}(d))$ and a stress field $\sigma \in L^2(Y; \mathrm{Sym}(d))$ which satisfy small-strain kinematic compatibility

$$\varepsilon = E + \nabla^s u \tag{54}$$

for some homogeneous strain $E \in \mathrm{Sym}(d)$, a periodic displacement fluctuation field $u \in H^1_{\mathrm{per}}(Y)^d$ and the symmetrized gradient operator ∇^s, stress equilibrium at the microscale without body forces

$$\mathrm{div}\, \sigma = 0 \tag{55}$$

the constitutive law

$$\sigma(x) = S(x, \varepsilon(x)) \quad \text{for almost all} \quad x \in Y \tag{56}$$

and the imposed conditions

$$\mathbb{P} : \langle \varepsilon \rangle_Y = \overline{\varepsilon} \quad \text{and} \quad \mathbb{Q} : \langle \sigma \rangle_Y = \overline{\sigma} \tag{57}$$

on the spatial averages of strain and stress, where the operator $\langle \cdot \rangle_Y$ computes the spatial mean of the quantity in brackets.

The basis for the Eyre–Milton method [35] and its descendants is the equivalence of the Equations (54–57) to the validity of the Eyre–Milton equation

$$P = 2\,\mathbb{C}^0 : \overline{\varepsilon} + 2\,\overline{\sigma} + \mathbb{Y} : Z^0(P) \tag{58}$$

for the plus-polarization field

$$P = \sigma + \mathbb{C}^0 : \varepsilon \tag{59}$$

where $\mathbb{C}^0 = \alpha_0\,\mathrm{Id}$ is a reference material with an arbitrary Young's modulus $\alpha_0 > 0$ and where we define the tensor operator

$$\mathbb{Y} = \mathrm{Id} - 2\mathbf{\Gamma} - 2\mathbb{Q}\circ\langle\cdot\rangle_Y \in L(L^2(\mathrm{Sym}(d))) \quad \text{with}$$
$$\mathbf{\Gamma} = \nabla^s(\mathrm{div}\,\nabla^s)^\dagger\mathrm{div} \tag{60}$$

as well as the "nonlinear reflection" operator

$$Z^0 : L^2(Y; \mathrm{Sym}(d)) \to L^2(Y; \mathrm{Sym}(d))$$
$$Z^0(P) = J^0(P) - K^0(P) \tag{61}$$

which involves the operators

$$J^0(P) = P - K^0(P) \tag{62}$$

$$K^0(P) = \mathbb{C}^0 : (S + \mathbb{C}^0)^{-1}(P) \tag{63}$$

The latter condition means that the equation

$$P = K^0(P) + S\big(\mathbb{D}^0 : K^0(P)\big) \quad \text{holds for all}$$
$$P \in L^2(Y; \mathrm{Sym}(d)) \quad \text{and with} \quad \mathbb{D}^0 = \big(\mathbb{C}^0\big)^{-1} \tag{64}$$

The operator (63) is well-defined due to the strong monotonicity of the operator $\mathbb{C}^0 + S$.

For the equivalence of the Equations (54–57) and the Eyre–Milton equation in the nonlinear setting, we refer to Schneider et al. [41].

Let us discuss the emergence of the operators (62) and (63) a little bit as they are central to the ensuing analysis. The operators J^0 and K^0 are defined in such a way that if the polarization (59) comes from a stress-strain pair which satisfies the constitutive law (56), that is,

$$P = \sigma + \mathbb{C}^0 : \varepsilon \quad \text{with} \quad \sigma = S(\cdot, \varepsilon) \tag{65}$$

then we can recover both the stress and the strain field via

$$\sigma = J^0(P) \quad \text{and} \quad \mathbb{C}^0 : \varepsilon = K^0(P) \tag{66}$$

Conversely, for *any* given polarization field $P \in L^2(Y; \mathrm{Sym}(d))$, defining a strain and a stress field by Equation (66) permits to decompose the given polarization field P into a pair of stress and strain fields which are related by the constitutive law. With this observation at hand, the action of the Z^0 operator (61) becomes

$$Z^0(P) = \sigma - \mathbb{C}^0 : \varepsilon \quad \text{in the decomposition (65)} \tag{67}$$

These considerations are also true in the pore space, where the definitions (62) and (63) imply the equations

$$J^0(P)(x) = 0 \quad \text{and} \quad K^0(P)(x) = P(x), \quad x \in Y_p. \tag{68}$$

In the skeleton $Y \setminus Y_p$, both operators J^0 and K^0 are strongly monotone. More precisely, the inequalities

$$\big[J^0(P_1)(x) - J^0(P_2)(x)\big] : \big(P_1(x) - P_2(x)\big)$$
$$\geq \frac{\alpha_-}{\alpha_- + \alpha_0}\,\big\|P_1(x) - P_2(x)\big\|^2, \quad \text{a.a. } x \in Y \setminus Y_p \tag{69}$$

and

$$\big[K^0(P_1)(x) - K^0(P_2)(x)\big] : \big(P_1(x) - P_2(x)\big)$$
$$\geq \frac{\alpha_0}{\alpha_+ + \alpha_0}\,\big\|P_1(x) - P_2(x)\big\|^2, \quad \text{a.a. } x \in Y \setminus Y_p \tag{70}$$

hold for arbitrary fields $P_1, P_2 \in L^2(Y; \mathrm{Sym}(d))$ in terms of the constants $\alpha_\pm$ arising in the assumed conditions (50) as well as (51) and the reference material constant α_0. The validity of the estimates (69) and (70) follows directly from general considerations of convex analysis [58] by identifying the operator K^0 as a resolvent operator [51], §2.4, whereas the operator J^0 corresponds to a reflected resolvent operator [51], §2.5.

The classical analysis of the nonlinear Eyre–Milton scheme [35, 40, 41], that is, in case of vanishing pore space, rests upon the estimate

$$\big\|Z^0(P_1)(x) - Z^0(P_2)(x)\big\|$$
$$\leq \rho(\alpha_0)\,\big\|P_2(x) - P_2(x)\big\|, \quad \text{a.a. } x \in Y \setminus Y_p \tag{71}$$

for the contraction constant

$$\rho(\alpha_0) = \max\!\left(\left|\frac{\alpha_- - \alpha_0}{\alpha_- + \alpha_0}\right|, \left|\frac{\alpha_+ - \alpha_0}{\alpha_+ + \alpha_0}\right|\right) \tag{72}$$

of the operator Z^0 on the skeleton, valid for arbitrary fields $P_1, P_2 \in L^2(Y; \mathrm{Sym}(d))$. The estimate (71) follows from general considerations of convex analysis, see Giselsson–Boyd [44].

Moreover, it is well known [35, 40, 41] that the reflection operator $\mathbb{Y}$ defined in Equation (60) is orthogonal, that is, the identity

$$\|\mathbb{Y} : \tau\|_{L^2} = \|\tau\|_{L^2} \quad \text{holds for any} \quad \tau \in L^2(Y; \mathrm{Sym}(d)) \tag{73}$$

where we use the L^2-norm associated to the inner product

$$(\tau, P)_{L^2} = \frac{1}{|Y|}\int_Y \tau : P\,dx, \quad \tau, P \in L^2(Y; \mathrm{Sym}(d)) \tag{74}$$

With these observations at hand, we consider the Hilbert space

$$H = L^2(Y; \mathrm{Sym}(d)) \tag{75}$$

and the fixed-point mapping (76) encoding the right-hand side of the Eyre–Milton Equation (58)

$$F : L^2(Y; \mathrm{Sym}(d)) \to L^2(Y; \mathrm{Sym}(d))$$
$$F(P) = 2\,\mathbb{C}^0 : \overline{\varepsilon} + 2\,\overline{\sigma} + \mathbb{Y} : Z^0(P) \tag{76}$$

Apparently, any fixed point of the mapping (76) corresponds to the solution of the Eyre–Milton Equation (58) and thus to a solution to the micromechanical problem (62) and (63) of interest.

Based on the observation

$$\|F(P_1) - F(P_2)\|_{L^2} = \|\mathbb{Y} : Z^0(P_1) - \mathbb{Y} : Z^0(P_1)\|_{L^2}$$
$$= \|Z^0(P_1) - Z^0(P_2)\|_{L^2} \quad (77)$$

where we used the definition (76) and the orthogonality (73), in case of vanishing pore space, one concludes the estimate

$$\|F(P_1) - F(P_2)\|_{L^2} \leq \rho(\alpha_0)\|Z^0(P_1) - Z^0(P_2)\|_{L^2} \quad (78)$$

As the prefactor (72) is less than unity for all reference-parameter choices $\alpha_0 > 0$, we have exposed the mapping F as a contraction mapping. In particular, the associated fixed-point method

$$P^{k+1} = F(P^k) \equiv 2\,\mathbb{C}^0 : \overline{\varepsilon} + 2\,\overline{\sigma} + \mathbb{Y} : Z^0(P^k) \quad (79)$$

converges linearly to the unique fixed point for any initial value P^0 as a consequence of the contraction mapping theorem.

In case of non-vanishing pore space, this simple analysis is no longer sufficient. The identity (77) only implies the non-expansivity estimate

$$\|F(P_1) - F(P_2)\|_{L^2} \leq \|P_1 - P_2\|_{L^2} \quad (80)$$

due to the identity

$$Z^0(P)(x) = -P(x), \quad x \in Y_p \quad (81)$$

valid in the pore space, see Equation (68).

The goal of the article at hand is to show that the damped fixed-point scheme

$$P^{k+1} = \gamma\,P^k + (1 - \gamma)F(P^k)$$
$$\equiv \gamma\,P^k + (1 - \gamma)\left[2\,\mathbb{C}^0 : \overline{\varepsilon} + 2\,\overline{\sigma} + \mathbb{Y} : Z^0(P^k)\right] \quad (82)$$

with non-trivial damping $\gamma \in (0, 1)$ converges on the closed subspace

$$H_0 = \left\{ P \in H \equiv L^2(Y; \mathrm{Sym}(d)) \,\middle|\, \mathrm{div}\,P = 0 \quad \text{in} \quad Y_p. \right\} \quad (83)$$

The course of action is to follow Section 3 and to establish the key estimate (30). Moreover, defining the residual mapping

$$R : L^2(Y; \mathrm{Sym}(d)) \to L^2(Y; \mathrm{Sym}(d)), \quad R(P) = P - F(P) \quad (84)$$

it will be shown that the space (83) is residual stable, that is, satisfies the property (28).

4.2 | Collecting the Relevant Identities and Estimates

The starting point of this investigation is the following useful expression for the residual (84)

$$R(P) = 2\,\mathbb{C}^0 : \tilde{\Gamma}^c : (\varepsilon - \overline{\varepsilon}) + 2\,\tilde{\Gamma} : (\sigma - \overline{\sigma}) \quad (85)$$

involving the complementary orthogonal projectors

$$\tilde{\Gamma} : P = \Gamma : P + \mathbb{Q} : \langle P \rangle_Y \quad \text{and} \quad \tilde{\Gamma}^c : P = P - \tilde{\Gamma} : P \quad (86)$$

as well as the fields

$$\sigma = J^0(P) \quad \text{and} \quad \varepsilon = \mathbb{D}^0 : K^0(P) \quad (87)$$

The formula (85) follows by elementary algebraic manipulations. For the convenience of the reader, the result is recalled in Appendix A1.

The representation formula (85) is quite useful, essentially for two reasons. For a start, the formula permits us to show the stability (28) of the linear subspace (83) under the action of the residual mapping (85). A direct consequence of the definition (60) of the operator $\tilde{\Gamma}$ is the simple formula

$$\mathrm{div}\,\tilde{\Gamma} : \tau = \mathrm{div}\,\tau, \quad \text{valid for any} \quad \tau \in L^2(Y; \mathrm{Sym}(d)) \quad (88)$$

which directly implies the complementary identity

$$\mathrm{div}\,\tilde{\Gamma}^c : \tau = \mathrm{div}\,(\tau - \tilde{\Gamma} : \tau) = \mathrm{div}\,\tau - \underbrace{\mathrm{div}\,\tilde{\Gamma} : \tau}_{=\mathrm{div}\,\tau} = 0 \quad (89)$$

Then, the representation formula (85) implies the identity

$$\mathrm{div}\,R(P) = 2\,\mathrm{div}\,\tilde{\Gamma}^c : \mathbb{C}^0 : (\varepsilon - \overline{\varepsilon}) + 2\,\mathrm{div}\,\tilde{\Gamma} : (\sigma - \overline{\sigma})$$
$$= 2\,\mathrm{div}\,(\sigma - \overline{\sigma}) = 2\,\mathrm{div}\,\sigma \quad (90)$$

where we used that the imposed stress $\overline{\sigma}$ is constant. Thus, we have the implication

$$\mathrm{div}\,R(P)(x) = 2\,\mathrm{div}\,\underbrace{\sigma(x)}_{=0} = 0 \quad \text{for} \quad x \in Y_p \quad (91)$$

In particular, the linear subspace (83) is stable under the action of residual mapping (85).

The second use of the representation formula (85) is in establishing the following key estimate

$$\frac{1}{2}\left(R(P_1) - R(P_2), P_1 - P_2\right)_{L^2}$$
$$\geq \frac{\alpha_0}{\alpha_+ + \alpha_0} \frac{1}{|Y|} \int_Y \left\|\tilde{\Gamma}^c : (P_1 - P_2)\right\|^2 dx$$
$$+ \frac{\alpha_-}{\alpha_- + \alpha_0} \frac{1}{|Y|} \int_{Y \setminus Y_p} \left\|\tilde{\Gamma} : (P_1 - P_2)\right\|^2 dx \quad (92)$$

which holds for arbitrary fields $P_1, P_2 \in L^2(Y; \mathrm{Sym}(d))$. In the case of linear elasticity and for pure strain loading, the lower bound (92) was established by Sab and co-workers [49]. The nonlinear case requires additional ideas, which we collect in Appendix A2.

The estimate (92) is rather close to the desired monotonicity estimate (30). However, the integral of the second term does not cover the pore space. To cope with this shortcoming, another estimate

is required. More precisely, there is a constant $\delta \in (0, 1]$, s.t. for any homogeneous strain field $\overline{T}$ and an arbitrary displacement fluctuation field $\boldsymbol{u} \in H^1_{\text{per}}(Y)^d$ which satisfies the PDE

$$\text{div } \nabla^s \boldsymbol{u} = \boldsymbol{0} \quad \text{in the pore space} \quad Y_p \qquad (93)$$

the estimate

$$\int_{Y \backslash Y_p} \left\| \overline{T} + \nabla^s \boldsymbol{u} \right\|^2 dx \geq \delta \int_Y \left\| \overline{T} + \nabla^s \boldsymbol{u} \right\|^2 dx \qquad (94)$$

holds, whose derivation is contained in Appendix A3.

4.3 | The Damped Eyre–Milton Method and Porous Microstructures

In this section, we are concerned with the micromechanical problem and how the damped Eyre–Milton method can be used to solve it. The following holds:

1. There is a unique solution $\boldsymbol{P}^* \in H_0$, that is, with div $\boldsymbol{P}^* = \boldsymbol{0}$ in the pore space Y_p, of the Eyre–Milton Equation (58).

2. For any starting point $\boldsymbol{P}^0 \in H_0$ and a non-trivial damping factor $\gamma \in (0, 1)$, the associated damped Eyre–Milton iterative scheme (79) converges linearly with the estimate

$$\begin{aligned} &\| \boldsymbol{P}^{k+1} - \boldsymbol{P}^* \|_{L^2} \\ &\leq \sqrt{1 - 2c_- \gamma (1 - \gamma)} \, \| \boldsymbol{P}^k - \boldsymbol{P}^* \|_{L^2}, \quad k = 0, 1, 2, \dots \end{aligned} \qquad (95)$$

and the constant

$$c_- = 2 \min \left(\frac{\alpha_0}{\alpha_+ + \alpha_0}, \frac{\alpha_- \delta}{\alpha_- + \alpha_0} \right) \qquad (96)$$

where α_0 denotes the reference-material constant, $\alpha_\pm$ stands for the strong monotonicity (50) and Lipschitz constant (51) of the stress operator in the skeleton and the constant $\delta \in (0, 1]$ arises in the Korn-type lower bound (94).

3. The bound (95) is optimized for $\gamma = 1/2$, that is, the method which is equivalent to what was introduced by Michel, Moulinec, and Suquet [36, 37] as the "augmented Lagrangian scheme". In this case, the contraction estimate (95) becomes

$$\begin{aligned} \| \boldsymbol{P}^{k+1} - \boldsymbol{P}^* \|_{L^2} &\leq \sqrt{1 - \min \left(\frac{\alpha_0}{\alpha_+ + \alpha_0}, \frac{\alpha_- \delta}{\alpha_- + \alpha_0} \right)} \\ &\quad \| \boldsymbol{P}^k - \boldsymbol{P}^* \|_{L^2} \quad k = 0, 1, 2, \dots \end{aligned} \qquad (97)$$

These assertions follow directly from the abstract derivations provided in section 3. We have already established that the subspace (83) is stable under the action of the vector residual (84) and that the fixed-point mapping (76) is non-expansive (22), see Equation (80). It remains to establish the monotonicity estimate

$$\left(\boldsymbol{R}(\boldsymbol{P}_1) - \boldsymbol{R}(\boldsymbol{P}_2), \boldsymbol{P}_1 - \boldsymbol{P}_2 \right)_{L^2} \geq c_- \| \boldsymbol{P}_1 - \boldsymbol{P}_2 \|^2_{L^2} \qquad (98)$$

for all fields $\boldsymbol{P}_1, \boldsymbol{P}_2 \in H_0$ and the constant (96).

The point of departure is the key estimate (92), which is valid for any pair of fields $\boldsymbol{P}_1$ and $\boldsymbol{P}_2$. In case both fields $\boldsymbol{P}_1$ and $\boldsymbol{P}_2$ belong to the subspace H_0, the estimate

$$\frac{1}{|Y|} \int_{Y \backslash Y_p} \left\| \tilde{\boldsymbol{\Gamma}} : (\boldsymbol{P}_1 - \boldsymbol{P}_2) \right\|^2 dx \geq \delta \frac{1}{|Y|} \int_Y \left\| \tilde{\boldsymbol{\Gamma}} : (\boldsymbol{P}_1 - \boldsymbol{P}_2) \right\|^2 dx \qquad (99)$$

holds. In fact, writing

$$\tilde{\boldsymbol{\Gamma}} : (\boldsymbol{P}_1 - \boldsymbol{P}_2) = \boldsymbol{\Gamma} : (\boldsymbol{P}_1 - \boldsymbol{P}_2) + \mathbb{Q} : \langle \boldsymbol{P}_1 - \boldsymbol{P}_2 \rangle_Y \equiv \overline{\mathbb{T}} + \nabla^s \boldsymbol{u} \qquad (100)$$

for the fields

$$\overline{\mathbb{T}} = \mathbb{Q} : \langle \boldsymbol{P}_1 - \boldsymbol{P}_2 \rangle_Y \quad \text{and} \quad \boldsymbol{u} = (\text{div } \nabla^s)^\dagger \text{div } (\boldsymbol{P}_1 - \boldsymbol{P}_2) \qquad (101)$$

we may apply the estimate (94) to deduce

$$\begin{aligned} &\int_{Y \backslash Y_p} \left\| \tilde{\boldsymbol{\Gamma}} : (\boldsymbol{P}_1 - \boldsymbol{P}_2) \right\|^2 dx \\ &= \int_{Y \backslash Y_p} \left\| \overline{\mathbb{T}} + \nabla^s \boldsymbol{u} \right\|^2 dx \geq \delta \int_Y \left\| \overline{\mathbb{T}} + \nabla^s \boldsymbol{u} \right\|^2 dx \qquad (102) \\ &= \delta \int_Y \left\| \tilde{\boldsymbol{\Gamma}} : (\boldsymbol{P}_1 - \boldsymbol{P}_2) \right\|^2 dx \end{aligned}$$

which is the desired estimate (98). Here, we used the simple identity (88) to see that

$$\text{div } \nabla^s \boldsymbol{u} = \text{div } \boldsymbol{\Gamma} : (\boldsymbol{P}_1 - \boldsymbol{P}_2) = \text{div } (\boldsymbol{P}_1 - \boldsymbol{P}_2) = \boldsymbol{0} \quad \text{in} \quad Y_p. \qquad (103)$$

We comment on the obtained results.

1. The obtained assertions confirm previous computational experiments [46] which suggest that the non-damped Eyre–Milton scheme (79) does not (always) converge for porous materials, whereas non-trivial damping with a factor $\gamma \in (0, 1)$ leads to convergence.

2. Sab et al. [49] analyzed the case of linear composites with pure strain loading, that is, $\mathbb{Q} = \boldsymbol{0}$, and proposed an Eyre–Milton type scheme with a damping parameter γ_k which may change from one iteration to the next and which is chosen from an extremum principle. The work at hand shows that such a procedure is not necessary for convergence. Rather, selecting an iteration-independent damping factor is sufficient to ensure convergence. Whether choosing the damping factor adaptively may be advantageous is another matter, however.

3. We established the arguments in the continuous setting, that is, not factoring in the effect of the discretization scheme used. However, it is well known that the discretization scheme has a strong effect on the convergence behavior of FFT-based schemes [5, 7]. In the context of primal formulations and porous materials, certain finite difference and finite element discretizations [6–8, 59] render the typical iterative schemes [1, 22, 27] convergent, whereas the Fourier-type discretizations [2, 12–14] may imply divergence [5, 7]. Similar observations were made in the context of polarization methods [26, 46, 49].

4. The convergence rate (97) of the iterative scheme depends on the choice of the reference constant α_0. The contraction factor (97) is minimized w.r.t. the value α_0 precisely if the monotonicity constant (96) is maximized. This is the case provided the identity

$$\frac{\alpha_0}{\alpha_+ + \alpha_0} = \frac{\alpha_- \delta}{\alpha_- + \alpha_0} \quad (104)$$

holds. Solving this quadratic equation for $\alpha_0 > 0$ gives the solution

$$\alpha_0^* = \sqrt{\frac{(1-\delta)^2}{4} \alpha_-^2 + \alpha_- \alpha_+ \delta} - \frac{1-\delta}{2} \alpha_- \quad (105)$$

Thus, in case of vanishing porosity, that is, $\delta = 1$, we recover the optimal reference constant

$$\alpha_0^* = \sqrt{\alpha_+ \alpha_-} \quad (106)$$

that was established previously [35, 40, 41]. For the other extreme, that is, strong porosity, we expect the constant $\delta \ll 1$ to be rather small, and we are interested in this case. By Taylor's theorem, we are led to the expansion

$$\alpha_0^* = \alpha_+ \delta + O(\delta^2) \quad (107)$$

In general, the optimal reference material α_0^* increases with the porosity constant δ, and lies in the interval $\left(0, \sqrt{\alpha_+ \alpha_-}\right]$.

5. In case of strong porosity and of a small porosity constant δ, the monotonicity constant (96) associated to the reference material (107) is

$$c_- \equiv 2 \frac{\alpha_- \delta}{\alpha_- + \alpha_+ \delta} = 2 \delta + O(\delta^2) \quad (108)$$

In particular, for prescribed tolerance, on the order of $1/\delta$ iterations are required for the damped Eyre–Milton scheme (82). In contrast, only $1/\sqrt{\delta}$ iterations are required for (Newton-)CG, see Schneider [48]. This means that either our estimates are not optimal or the damped Eyre–Milton method (82) is less effective for porous materials than the most efficient primal solvers [48].

6. The developments in this article involved a fixed reference material. However, as the optimal reference material choice (105) involves the parameter δ which is hard to estimate, more focus should be laid on adaptive parameter estimation techniques [45, 46].

5 | Computational Investigations

5.1 | Setup

The polarization schemes described in this paper were implemented in an existing in-house FFT-based micromechanics solver, written in Python with Cython extensions, using OpenMP for parallelization and the FFTW [60] library to apply the fast Fourier transform. All computational examples were run on a laptop with 32 GB RAM and an Intel Core i5 1.3 GHz processor.

In the following, polarization schemes are compared to primal and ADMM-based solvers. We resort to the convergence criteria presented in Schneider et al. [41]. These convergence criteria are based on the introduction of a Lippmann-Schwinger operator

$$\begin{aligned} \mathbf{\Lambda}(\varepsilon) = \varepsilon &+ (\Gamma^0 + \mathbb{D}^0 : \mathbb{Q} : \langle \cdot \rangle) : \\ &\left(\mathbf{S}(\cdot, \varepsilon) - \mathbb{C}^0 : \varepsilon\right) - \mathbf{E} - \mathbb{D}^0 : \mathbf{\Sigma} \end{aligned} \quad (109)$$

This Lippmann-Schwinger operator is equivalent to the residual operator introduced in (85). The difference between the two operators is the quantity which it acts upon. The operator (109) takes a strain field as input, whereas the residual (85) acts on a polarization (59). In formulas, the identity

$$\mathbf{R}(\mathbf{P}) = 2\mathbb{C}^0 : \mathbf{\Lambda}(\varepsilon) \quad \text{holds with} \quad \mathbf{P} = \mathbf{S}(\cdot, \varepsilon) + \mathbb{C}^0 : \varepsilon \quad (110)$$

The operator (109) quantifies the degree of kinematic compatibility of the strain ε, the equilibrium of the stress field, and the satisfaction of the macroscopic loading conditions.

For all solvers, we consider the residual

$$\text{res} = \frac{\|\mathbf{\Lambda}(\varepsilon)\|_{\mathbb{C}^0}}{\|\langle \boldsymbol{\sigma} \rangle_Y\|_{\mathbb{D}^0}} \quad (111)$$

where $\| \cdot \|_{\mathbb{C}^0}$ and $\| \cdot \|_{\mathbb{D}^0}$ denote the $\mathbb{C}^0$ and the $\mathbb{D}^0$ weighted L^2 inner products, respectively.

For primal solvers like the basic scheme, compatibility and the macroscopic strain conditions are directly enforced by the solver at every iteration. Hence, the residual (111) becomes

$$\text{res} = \frac{\left\|\Gamma^0 : \mathbf{S}(\cdot, \varepsilon) + \mathbb{D}^0 : \left(\langle \mathbf{S}(\cdot, \varepsilon) \rangle_Y - \mathbf{\Sigma}\right)\right\|_{\mathbb{C}_0}}{\|\langle \mathbf{S}(\cdot, \varepsilon^k) \rangle_Y\|_{\mathbb{D}_0}} \quad (112)$$

This quantity does not depend on the constant α_0 in the reference material $\mathbb{C}^0 = \alpha_0$ Id, see Schneider et al. [41]. In the following, the quantity defined in Equation (112) is used as the residual for primal schemes.

For polarization schemes in Eyre–Milton form (82)

$$\mathbf{P}^{k+1} = \gamma \, \mathbf{P}^k + (1 - \gamma)(\mathbf{P}^k - \mathbf{R}(\mathbf{P}^k)) = \mathbf{P}^k - (1 - \gamma)\mathbf{R}(\mathbf{P}^k) \quad (113)$$

one observes the identity

$$\frac{\|\mathbf{P}^{k+1} - \mathbf{P}^k\|_{\mathbb{D}^0}}{1 - \gamma} = \|\mathbf{R}(\mathbf{P}^k)\|_{\mathbb{D}^0} \quad (114)$$

Thus, the residual (111) takes the form

$$\text{res} = \frac{1}{2(1 - \gamma)} \frac{\|\mathbf{P}^{k+1} - \mathbf{P}^k\|_{\mathbb{D}_0}}{\|\langle \mathbf{S}(\cdot, \varepsilon^k) \rangle_Y\|_{\mathbb{D}_0}} \quad (115)$$

for polarization schemes (82). In particular, although the damping factor γ appears explicitly in the expression (115), the residual is independent of the damping factor.

For polarization schemes in the ADMM implementation [36, 37], the residual (111) may be expressed in the form

$$\text{res} = \frac{\|e^k - \varepsilon^{k+1/2}\|_{\mathbb{C}_0}}{\|\langle \sigma(\varepsilon^k) \rangle\|_{\mathbb{D}_0}} \qquad (116)$$

see Schneider [46].

For polarization schemes, the residual (111) depends on the reference material. However, the residual is the natural quantity which measures the contraction properties of the underlying fixed-point operator (76). Alternative residuals were considered, but come typically with additional computational overhead in the nonlinear or inelastic case.

Unless stated otherwise, all approaches are solved up to a tolerance tol $= 10^{-5}$ on the residual.

5.2 | A Sand-Core Microstructure

As a first example, we consider a sand-core microstructure, discretized by 256^3 voxels, represented in Figure 1a. The microstructure consists of 64 grains of sand with a volume fraction of 58.58%, held together by an inorganic binder with a volume fraction of 1.28%. It was generated by a variant of the mechanical contraction method initially proposed by Williams and Philipse [61], described in Schneider et al. [62]. The material parameters of the constituent materials are given in Table 1.

First, the behavior of the damped Eyre–Milton scheme (82) is investigated for three different discretizations: Moulinec–Suquet's spectral discretization based on trigonometric polynomials [1, 2], the rotated staggered grid [6] and the staggered grid discretization [7]. For all three discretizations, the reference material is chosen as $\alpha_0 = \sqrt{\alpha_+ \alpha_-}$, where α_- (resp. α_+) is the lowest non-zero (resp. highest) eigenvalue of the sand and binder's stiffness tensors. Results are presented for two damping factors: $\gamma = 0.25$ and $\gamma = 0.5$. For all discretizations, a vanishing damping factor $\gamma = 0$ led to divergence of the solver, while for damping factors $\gamma = 0.25$ and $\gamma = 0.5$, only the staggered grid shows linear convergence. The other two discretizations feature logarithmic convergence, failing to reduce the residual below 10^{-5} after 10,000 iterations. Willot's discretization leads to a $2.32.10^{-4}$ residual after 10,000 iterations for a damping factor of $\gamma = 0.25$ (resp. a $2.78.10^{-4}$ residual for a damping factor of $\gamma = 0.5$). Moulinec–Suquet's discretization leads to a residual of $1.21.10^{-3}$ (resp. $1.48.10^{-3}$) for the same number of iterations. Similar results, showing a more stable behavior for the staggered grid discretization than for the other two on porous microstructures, were reported for primal solvers [48]. Hence, the staggered grid discretization is used in the following examples.

As highlighted in Section 4.3, choosing the reference material $\alpha_0 = \sqrt{\alpha_+ \alpha_-}$ optimizes the theoretical bound on the convergence rate for non-porous microstructures, see Equation (95). Such an optimal choice can also be derived for porous materials, as shown in Equation (107). However it relies on a constant δ, which depends on the geometry of the microstructure and is difficult to estimate. Figure 2a compares various choices of reference material α_0:

- the arithmetic mean of the highest and lowest (zero in the porous case) eigenvalues $\alpha_0 = 0.5\alpha_+$;
- the geometric mean of the highest and lowest non-zero eigenvalues $\alpha_0 = \sqrt{\alpha_+ \alpha_-}$;
- the lowest non-zero eigenvalue $\alpha_0 = \alpha_-$;
- the highest eigenvalue $\alpha_0 = \alpha_+$;
- and the choice of reference material $\alpha_0 = \alpha_+/5$ case, investigated by Schneider [46] and which performs well in Monchiet and Bonnet [39].

For all of these choices, results are plotted for two different damping factors: $\gamma = 0.25$ and $\gamma = 0.5$.

TABLE 1 | Elastic properties for the sand grain microstructure.

	E (in GPa)	ν
Quartz sand [63, 64]	66.9	0.25
Inorganic water glass binder [65]	71.7	0.17
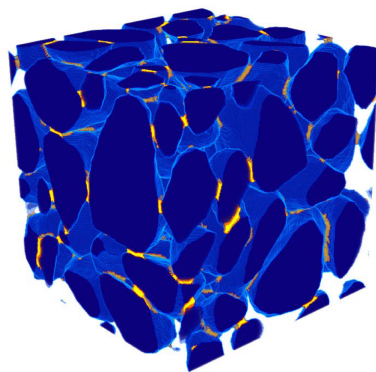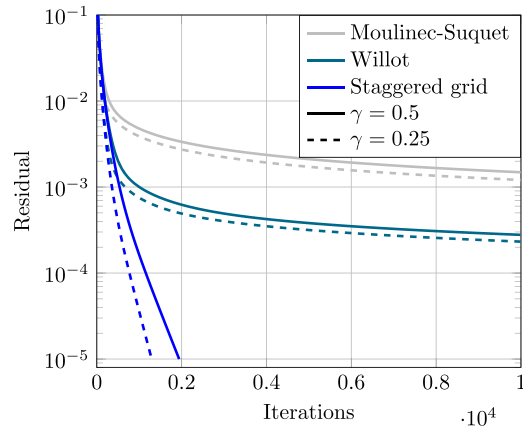
(a)
(b)

FIGURE 1 | A sand core microstructure. (a) Geometry of the microstructure; (b) Convergence for different discretizations.
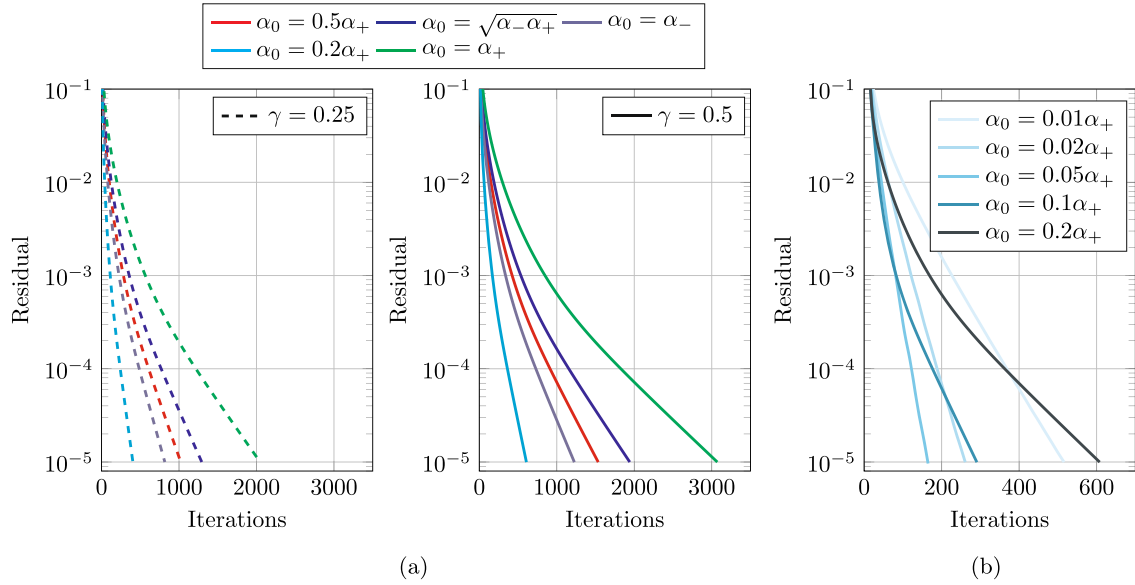
FIGURE 2 | Sand core microstructure: choice of the reference material. (a) Common choices of reference material, Damping factor: left $\gamma = 0.25$, right $\gamma = 0.5$; (b) Adjustment of the reference material, damping factor $\gamma = 0.5$.

From Figure 2a, it appears that considering the upper-bound eigenvalue α_+ as a reference material leads to the lowest asymptotic convergence rate, while considering the value $\alpha_0 = 0.2\alpha_+$ stemming from Monchiet–Bonnet's computational experiments [39] leads to the highest asymptotic convergence rate. We note that, in terms of values, the following relations hold for the present example:

$$0.2\alpha_+ \leq \alpha_- \leq 0.5\alpha_+ \leq \sqrt{\alpha_+ \alpha_-} \leq \alpha_+ \qquad (117)$$

Hence, the smallest of these five reference materials leads to the fastest convergence rate. This is consistent with Equation (107), from which we expect that the optimal reference material is only a fraction of the highest stiffness tensor eigenvalue: $\alpha_0 = \delta\alpha_+$, where the constant δ is small. In order to try to refine the estimate on the unknown parameter δ, several values were tested in Figure 2b, for a damping factor $\gamma = 0.5$. From this figure, it appears that a value $\delta = 0.05$ provides the reference material which maximizes the convergence rate and minimizes the number of iterations to reach a tolerance of 10^{-5}. It is also interesting to note that all cases present a superlinear convergence rate for the first dozens of iterations. However, such a superlinear phase is longer if the reference material is chosen too stiff than if it is too soft. As an example, the asymptotic convergence rate is around the same for the reference materials $\alpha_0 = 0.01\alpha_+$ and $\alpha_0 = 0.1\alpha_+$, however the latter converges to a tolerance of 10^{-5} in half as many iterations as the former. We also observe that a proper choice of the reference material has a significant effect on the iteration count required to reach the desired tolerance: for a damping factor $\gamma = 0.5$, choosing a reference material $\alpha_0 = \alpha_+$ leads to 18.6 more iterations that the present optimal choice $\alpha = 0.05\alpha_+$.

In Figure 3a, we study the effect of the damping factor on the convergence speed for a given reference material $\alpha_0 = 0.05\alpha_+$. It appears that all considered damping factors, from $\gamma = 0.01$ to $\gamma = 0.9$, lead to convergence. This result is consistent with the theoretical convergence analysis performed in Section 4.3, which

showed that any damping factor γ in the open interval $(0,1)$ should lead to linear convergence. From Figure 3a, the highest final convergence rate is reached for a damping factor $\gamma = 0.1$.

In order to compare the convergence rate of the DEM schemes investigated in Figure 3a to the convergence rate of primal solvers, Figure 3b shows the convergence behavior of the conjugate gradient method (abbreviated CG) introduced by Zeman et al. [27] and of the primal Barzilai-Borwein approach [22] (abbreviated BB). In the present example, the CG solver outperforms all DEM approaches in terms of convergence rate and of number of iterations to convergence. In particular, it converges to a tolerance of 10^{-5} in 74% less iterations than the DEM approach with a damping factor $\gamma = 0.5$, and in 7% less iterations than the $\gamma = 0.1$-version of DEM. This result is consistent with the convergence rate estimates for CG and DEM, recalled in remark 5., Section 4.3. The Barzilai-Borwein approach reaches the prescribed tolerance in more iterations than the DEM approaches featuring a damping factor comprised between 0.05 and 0.25. However, it outperforms the DEM approaches with a damping factor of 0.01 or greater than 0.5 in terms of iteration count.

For practical applications, it is of interest to determine the solvers parameters that lead to the minimum number of iterations to reach a given tolerance, even though these parameters do not necessarily yield the optimal convergence rate. For that purpose, Figure 3c reports the number of iterations required to reach tolerance tol $= 10^{-5}$ as a function of the reference material and of the damping factor. A damping factor of $\gamma = 0.05$ is optimal for a reference material exceeding $0.05\alpha_+$, while a damping factor of $\gamma = 0.1$ leads to a lower number of iterations for a reference material inferior to $0.05\alpha_+$. For all investigated reference materials, considering a damping factor $\gamma = 0.25$ increases the number of iterations by 5 to 27%. A damping factor of $\gamma = 0.5$ performs worse and leads to the number of iterations increased by 46 to 91%. From Figure 3c, it also appears that the optimal reference material is almost independent of the damping factor.
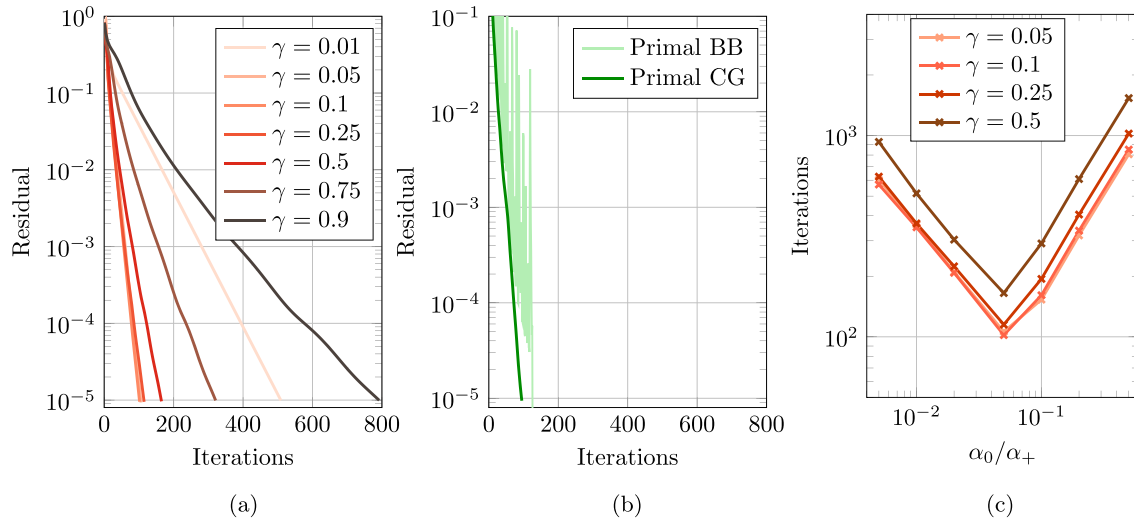
FIGURE 3 | Sand core microstructure: influence of the damping factor on convergence and comparison to primal approaches. (a) DEM solver: residual for a reference material $\alpha_0 = 0.05\alpha_+$; (b) Primal solvers: residual; (c) DEM solver: iteration count to reach a residual of 10^{-5}.

TABLE 2 | Iteration counts for various adaptive polarization approaches.

	$\gamma = 0.25$		$\gamma = 0.5$	
Actualization strategy	**Iterations**	**Final value of the reference material**	**Iterations**	**Final value of the reference material**
Barzilai-Borwein	175	$\alpha_0 = 4\,247$ MPa $(0.034\alpha_+)$	236	$\alpha_0 = 4\,347$ MPa $(0.034\alpha_+)$
Residual Balancing	914	$\alpha_0 = 59\,837$ MPa $(0.45\alpha_+)$	384	$\alpha_0 = 14\,959$ MPa $(0.11\alpha_+)$
Averaging	171	$\alpha_0 = 11\,920$ MPa $(0.089\alpha_+)$	257	$\alpha_0 = 11\,921$ MPa $(0.089\alpha_+)$

In Figures 2b and 3c, we performed a trial-and-error procedure to find the reference material leading to the fastest convergence. It is however tedious to perform such a fine-tuning of the reference material for every FFT simulation. Therefore, adaptive step-size strategies come in handy. In the following, we take advantage of the equivalence between the damped Eyre–Milton scheme and ADMM approaches [38, 40, 41] to resort to adaptive strategies developed for ADMM [45, 46]. We add to our investigations the Barzilai-Borwein [21] approach proposed by Xu et al. [66, 67], the residual balancing approach from He et al. [68] and the averaging approach presented by Lorentz and Tran-Dinh [69]. Table 2 records the number of iterations for those three adaptive approaches and for two damping factors: $\gamma = 0.25$ and $\gamma = 0.5$. All adaptive step-size strategies lead to convergence within less than 1,000 iterations. The most efficient one in the example at hand is the averaging strategy with a damping factor $\gamma = 0.25$, closely followed by the Barzilai-Borwein strategy, also for $\gamma = 0.25$. The residual balancing strategy is the only one where a damping factor $\gamma = 0.5$ leads to a lower number of iterations than a damping factor $\gamma = 0.25$. We also note that the best adaptive strategy still performs worse than a finely tuned constant reference material. Having a look at the final value of the reference material for all three strategies, it appears that the

efficiency of the strategy increases with the proximity to the best constant reference material.

As a conclusion to this first example on a quite challenging microstructure, it seems that an aggressive strategy, both in terms of the reference material and of the damping factor, leads to fast convergence of the damped Eyre–Milton scheme. For an optimal choice of these two parameters, the damped Eyre–Milton scheme exhibits performances comparable to the fastest available primal solvers.

5.3 | An Open-Cell Foam

As a second example, we consider the foam structure represented in Figure 4a. To generate such a microstructure, we followed the procedure proposed by Redenbach [70]. A random Laguerre tesselation is created first. Then, the edges of the Laguerre cells are thickened to give rise to a truss network. The final porosity is 80%, which makes FFT-based homogenization quite challenging. We furnished the solid material composing the microstructure with the isotropic properties of aluminum extracted from Segurado et al. [71], that is, a Young's modulus $E = 75$ GPa and a Poisson ratio $\nu = 0.3$. The microstructure is subjected to a uniaxial strain loading of 0.1% in the x-direction.
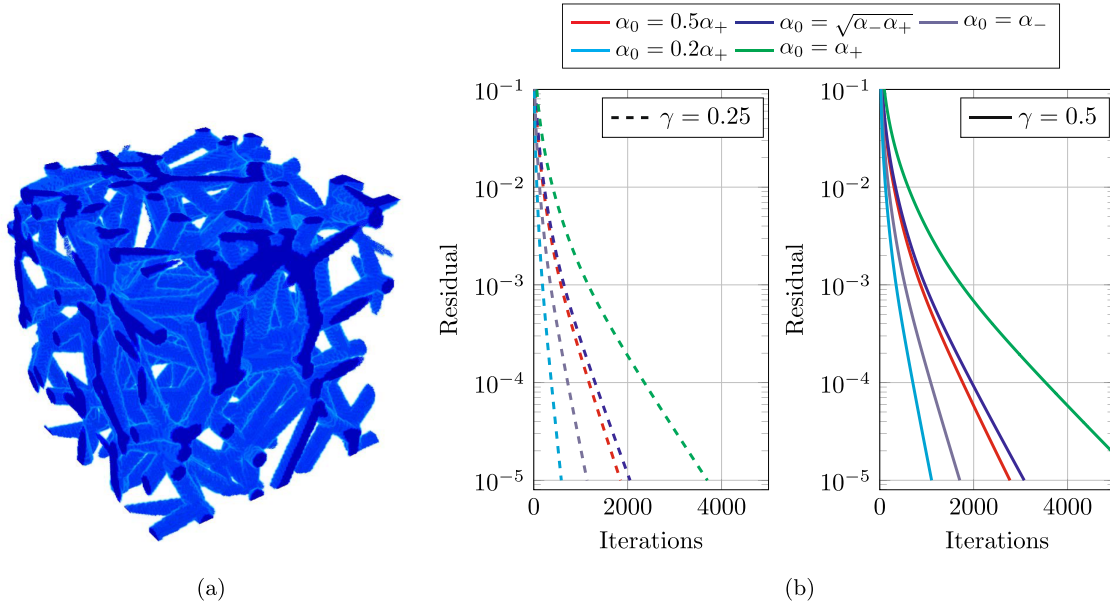
FIGURE 4 | Porous foam microstructure. (a) Geometry of the microstructure; (b) Evolution of the residual for various choices of constant reference material. Damping factor: left: $\gamma = 0.25$, right: $\gamma = 0.5$.
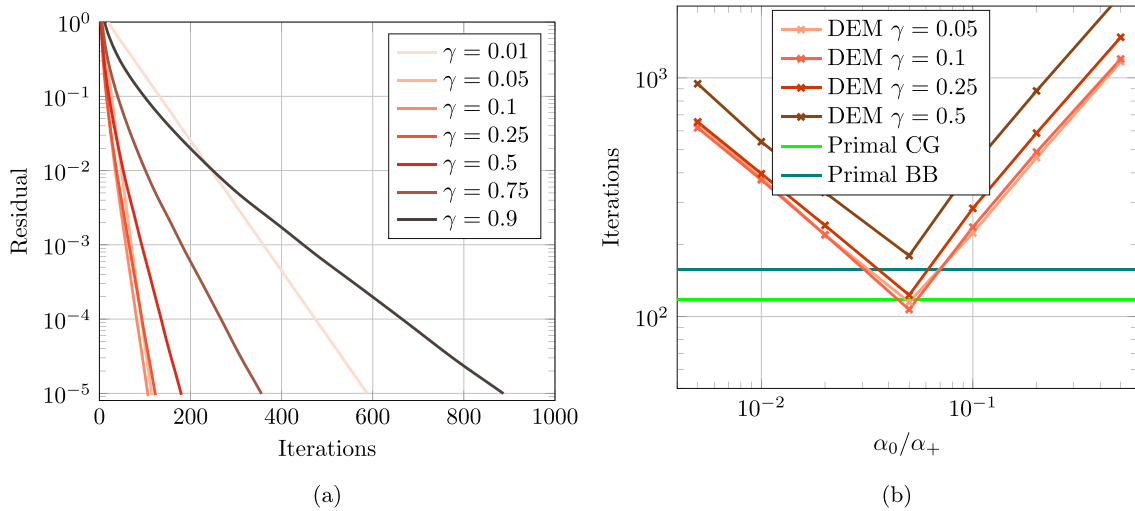

FIGURE 5 | Foam microstructure: influence of the damping factor on the convergence. (a) Evolution of the residual for a reference material $\alpha_0 = 0.2\alpha_+$; (b) Iteration count to reach a tolerance tol $= 10^{-5}$.

Different usual choices of reference material are investigated in Figure 4b. Among those choices, the strategy leading to the highest convergence rate is a reference material $\alpha_0 = 0.2\alpha_+$. We also note that the convergence rate for a given reference material is always lower with a damping factor $\gamma = 0.25$ than for $\gamma = 0.5$.

From Figure 5a, it appears that all investigated damping factors, from 0.01 to 0.9, lead to linear convergence. A damping factor $\gamma = 0.05$ minimizes the final convergence rate. Choosing a damping factor lower than this value reduces the length of the superconvergence phase at the beginning, while choosing a higher one still allows for superconvergence at the beginning but reduces the asymptotic convergence rate. We also note that, as hinted in Section 4.3, using damping factors greater than 0.5 is not favorable in terms of convergence rate.

Figure 5b reports investigations on the iteration count to reach a tolerance tol $= 10^{-5}$ for various damping factors and reference materials. The optimal reference material for this example is $\alpha_0 = 0.05\alpha_+$. As for the previous example, the optimal reference material is almost insensitive to the value of the damping factor. A damping factor $\gamma = 0.1$ leads to the lowest number of iterations for the optimal reference material, and may be outperformed by the value $\gamma = 0.05$ if the reference material is chosen too stiff, that is, exceeding the optimal one. Figure 5b also contains the results obtained by two primal solvers: CG [27] and primal BB [22]. Contrary to the previous example, the polarization schemes outperform the primal solvers in terms of iteration count for a reference material $\alpha_0 = 0.05\alpha_+$ and damping factors $\gamma = 0.05$ and $\gamma = 0.1$. The DEM scheme with a damping factor $\gamma = 0.25$ and $\gamma = 0.5$ is outperformed by

CG however, as it could be expected from the estimate derived in Section 4.3.

5.4 | A Porous Short Glass-Fiber Reinforced Polyamide

As a third example, we move out of the elastic setting and take into account materials with inelastic behavior. We investigate a fiber microstructure, presented in Figure 6a. Such a microstructure is composed of an elastoplastic polyamide matrix, reinforced by 150 μm-long, elastic glass fibers of diameter 10 μm with a 15% volume fraction, aligned in the x-direction. The matrix also contains 25 μm pores with a 1% volume fraction. The microstructure was generated using the sequential addition and migration algorithm [72, 73], and discretized by 256^3 voxels.

While the fibers are considered to behave elastically, the matrix is supposed to follow a J_2-elastoplastic material model with linear-exponential hardening:
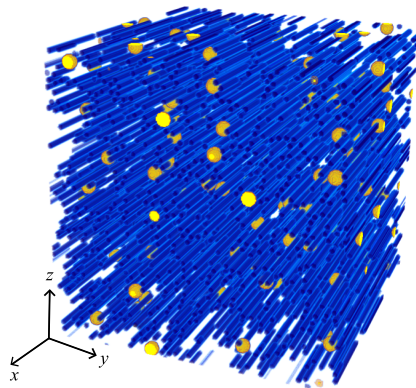
$$\sigma_0(p) = \sigma_Y + k_1 p + k_2(1 - \exp(-mp)) \tag{118}$$

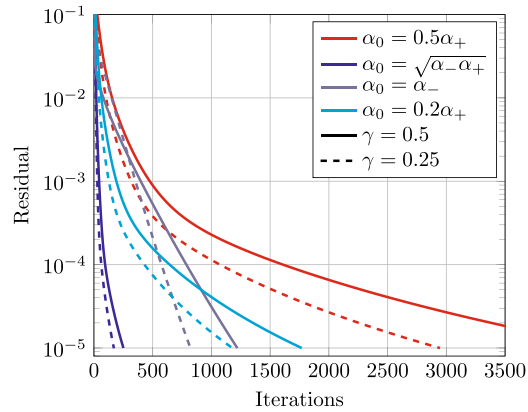All material parameters, extracted from Doghri et al. [74], are gathered in Table 3.

First, a uniaxial extension of 1% in x-direction is applied as a single-step loading.

Figure 6b records the convergence of the damped Eyre–Milton approach for different usual choices of reference materials and damping factors. With the considered material and considering a single-step loading, the following relations hold:

$$\alpha_- < \sqrt{\alpha_+ \alpha_-} < 0.2\alpha_+ < 0.5\alpha_+ < \alpha_+ \tag{119}$$

Figure 6b, shows that the polarization schemes converge linearly for all considered scenarios. In the present case, the highest convergence rate is obtained for the choice of reference material $\alpha_0 = \sqrt{\alpha_+ \alpha_-}$. This observation contrasts with the two previous examples and tends to indicate that the porosity constant is quite close to $\delta = 1$. A reference material $\alpha_0 = \alpha_-$ is too soft and leads to a too large step-size, while all other choices are too stiff. Once again, a damping factor $\gamma = 0.25$ leads to slightly less iterations than $\gamma = 0.5$, for all considered reference materials.

Figure 7a represents the convergence speed for various damping factors and a reference material $\alpha_0 = \sqrt{\alpha_+ \alpha_-}$. As for the previous two examples, the damped Eyre–Milton scheme converges linearly for all damping factors investigated. A damping factor of $\gamma = 0.05$ or $\gamma = 0.1$ enables faster convergence and a higher convergence rate. We also note that, for this specific example, the classical undamped Eyre–Milton scheme converges. This might be due to the low volume fraction and the regular shape of the pores.

Because the choice of reference material is non-trivial, it is of interest to resort to adaptive approaches as used for the sand core microstructure in Section 5.2. Figure 7b reports on the convergence behavior of the three adaptive polarization approaches investigated in Section 5.2, namely Barzilai–Borwein [66, 67], residual balancing [68] and averaging [69] actualization rules, for two values of damping factor: $\gamma = 0.25$ and $\gamma = 0.5$. Comparing Figure 7a,b reveals that the DEM approaches, with a reference material $\alpha_0 = \sqrt{\alpha_+ \alpha_-}$ and a damping factor comprised between 0.05 and 0.5, outperform adaptive approaches in terms of the convergence rate and iteration count. The damped Eyre–Milton scheme with a damping factor $\gamma = 0.05$ leads to the highest convergence rate among polarization schemes. The residual balancing and the averaging strategies lead to between 450 and 900 iterations. Thus, these two adaptive polarization approaches require

(a)   (b)

FIGURE 6 | Porous short glass-fiber reinforced polyamide microstructure. (a) Geometry of the microstructure; (b) Evolution of the residual for various choices of constant reference materials.

TABLE 3 | Mechanical properties for the porous fiber microstructure [74].

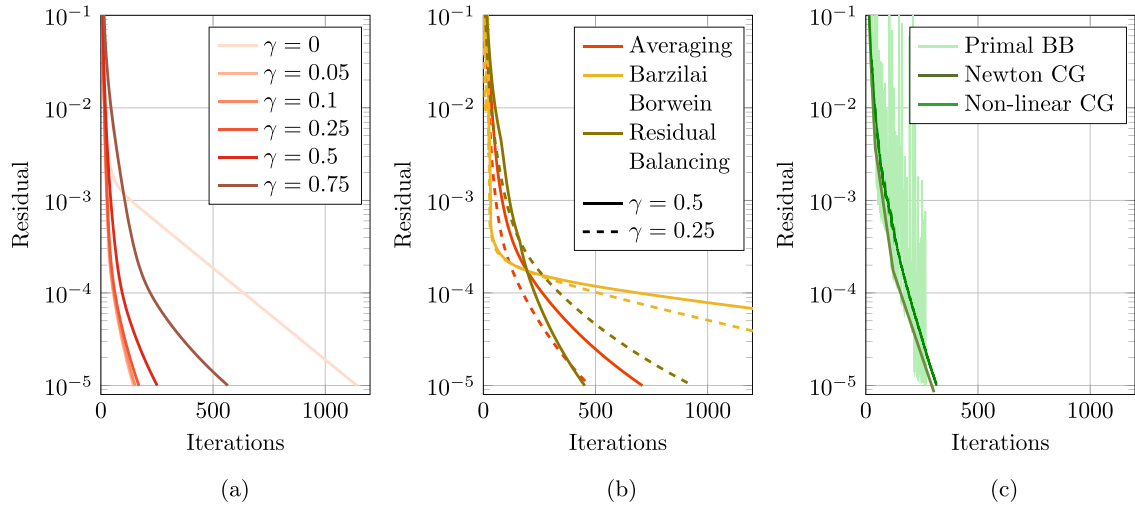| Glass fibers	$E = 72$ GPa	$v = 0.22$		
Polyamide	$E = 2.1$ GPa	$v = 0.3$	$\sigma_Y = 29$ MPa	$k_1 = 139$ MPa
matrix			$k_2 = 32.7$ MPa	$m = 319.4$

FIGURE 7 | Fiber microstructure: convergence behavior for various solvers. (a) DEM with a reference material $\alpha_0 = \sqrt{\alpha_+ \alpha_-}$; (b) Adaptive ADMM solvers; (c) Primal solvers.
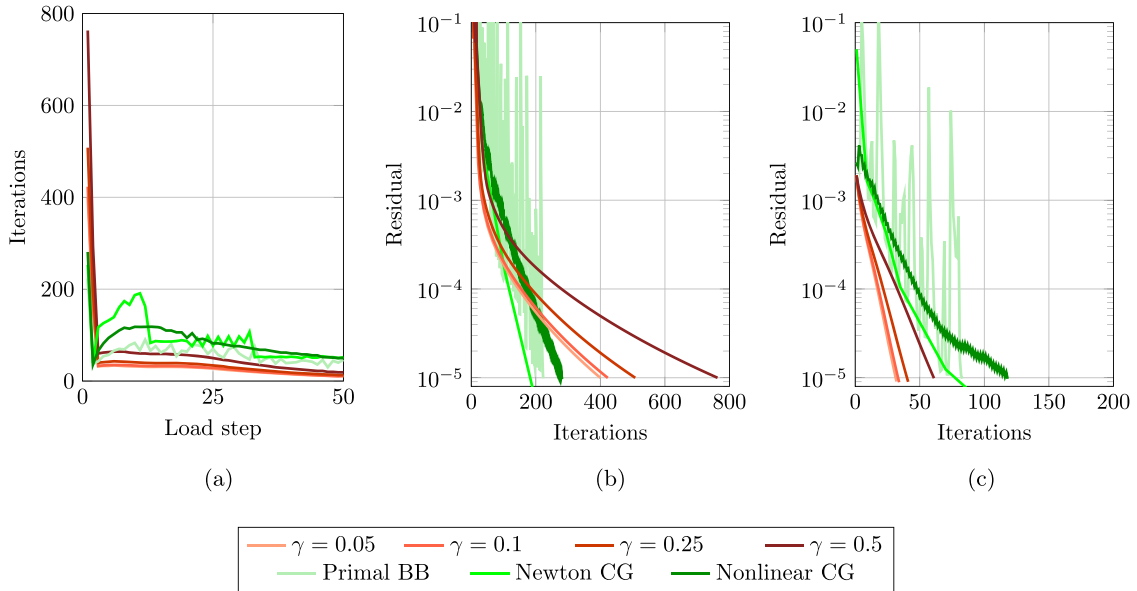

FIGURE 8 | Fiber microstructure: multiple load steps. (a) Iteration count per step for various solvers; (b) Convergence behaviour: First load step; (c) Convergence behaviour: Tenth load step.

around three to six times more iterations than the best polarization scheme, 1.5 to 3 times more than the primal approaches, but still less than most of the common constant strategies represented in Figure 6b. The Barzilai-Borwein rule leads to an excessively soft reference material $\alpha_0 = 30$ MPa and, hence, to a low convergence rate and the highest iteration count. In Figure 7c, three different primal solvers are also considered: the basic scheme with Barzilai-Borwein adaptive step-size [22], the nonlinear conjugate gradient method [28] and the Newton CG scheme [20, 30]. We note that the rate of convergence of all three primal approaches is higher than the rate of convergence of the $\gamma = 0.5$-DEM approach for low values of the residual, typically lower than 10^{-4}. For such values of the residual, the rate of convergence of the DEM approaches featuring damping ratios of $\gamma = 0.05$ to $\gamma = 0.25$ is similar to the one of primal approaches.

After considering a single large load step, we turn our attention to a different loading: a 5% strain is applied in 50 equidistant load steps in the x-direction. An affine extrapolation of the initial guess $\varepsilon^0(t_{n+1})$ is used for the load step t_{n+1}, as proposed by Moulinec and Suquet [2]:

$$\varepsilon^0(t_{n+1}) = \varepsilon^0(t_n) + \frac{t_{n+1} - t_n}{t_n - t_{n-1}} \left(\varepsilon(t_n) - \varepsilon(t_{n-1}) \right) \qquad (120)$$

where $\varepsilon(t_n)$ and $\varepsilon(t_{n-1})$ are the converged solution of the two previous steps. It should be noted that the lower-bound constant α_- depends on the hardening function, and its estimate is recomputed for each time step, see Schneider et al. [41].

Figure 8a shows the iteration count per loading step for four polarization approaches with various damping factors and

the fixed reference material $\alpha_0 = \sqrt{\alpha_+ \alpha_-}$. The three primal approaches investigated for the single-load-step loading, namely Barzilai Borwein, Newton CG and nonlinear CG, are also added for comparison. Interestingly, all four polarization approaches have a common pattern in terms of the number of iterations per step. The iteration count is rather high for the first to steps, from 400 for a damping factor $\gamma = 0.05$ to 763 for a damping factor $\gamma = 0.5$. It is divided by a factor of 12 to 13 by the third step, and then slowly decreases to reach between 11 iterations per step for a damping factor $\gamma = 0.05$ and 19 iterations per step for a damping factor $\gamma = 0.5$.

In terms of the average iteration count, the best primal approach is the Barzilai-Borwein scheme [22], with 60.8 iterations per step. The two other primal schemes, Newton-CG [20, 30] and nonlinear CG [28], perform significantly worse, with an average of 90.6 iterations/step for Newton CG and of 85.8 iterations/step for the nonlinear CG. The efficiency of the primal Barzilai-Borwein scheme relatively to CG schemes has already been outlined for inexpensive material laws [31], as it is the case here. The damped Eyre–Milton scheme outperforms all primal schemes, except for a damping factor $\gamma = 0.5$. For the example at hand, the best damping factor is $\gamma = 0.05$, with an average iteration count of 33.8 iterations/step.

We turn our attention to the convergence rate of the different methods. Figure 8b shows the convergence rate of the DEM and primal schemes for the first load step, while Figure 8c shows the same quantity for the tenth step. For the first iteration, all three primal solvers outperform the DEM schemes in terms of convergence rate and in terms of number of iterations to reach the tolerance tol = 10^{-5}. The opposite is true for the tenth loading step. Overall, the results presented in Figure 8 outline the performance of polarization methods compared to primal solvers in the nonlinear case.

5.5 | A Porous Metal Matrix Composite

For this last example, we consider a metal matrix composite, represented in Figure 9. This microstructure is composed of 33 ceramic inclusions with a volume fraction of 29.5%, blue-colored

in Figure 9 and 31 pores with a volume fraction of 0.5%, gold-colored in Figure 9. It was generated using the sequential addition and migration algorithm [72] and discretized by 128^3 voxels. The ceramic beads are assumed to be elastic while the aluminum matrix follows a J_2-elastoplastic material law with power-law hardening:

$$\sigma_0(p) = \sigma_Y + k \, p^m \tag{121}$$

All material parameters, extracted from Segurado et al. [71], are gathered in Table 4. The example at hand is challenging because of the exponent in the power-law hardening. Notably, the smallest eigenvalue α_- in the aluminum matrix goes to zero at high strains, which complicates the selection of an optimal reference material.

A uniaxial extension of 1% in the x-direction is applied via 50 equidistant loading steps.

Figure 9b shows the number of iterations per step for various choices of reference material and a damping factor of $\gamma = 0.25$. From Figure 9b, it appears that the best choice of reference material is $\alpha_0 = \sqrt{\alpha_+ \alpha_-}$ from the third iteration onwards. What is striking is how, once again, an unwise choice of reference material makes the damped Eyre–Milton scheme completely uncompetitive. For instance, regarding Figure 9b, the average iteration count per load increment goes from 23.3 for a reference material $\alpha_0 = \sqrt{\alpha_+ \alpha_-}$ to 180.0 for a reference material $\alpha_0 = \alpha_+$. From this example and the one presented in Section 5.4, it seems that a reference material $\alpha_0 = \sqrt{\alpha_+ \alpha_-}$ is an acceptable choice for porous microstructures with a low volume fraction of pores and a regular pore shape. For such a value of reference material, the damping factor leading to the lowest number of iterations is either $\gamma = 0.05$ or $\gamma = 0.1$ depending on the step considered, see Figure 10a. A damping factor $\gamma = 0.5$ leads to 72% more iterations on average, while $\gamma = 0.25$ leads to only 18% more iterations.

Figure 10 compares the convergence behavior of the DEM approaches with various damping factors to the behavior of the three primal schemes investigated in Section 5.4: Barzilai–Borwein [22], Newton CG [20, 30] and nonlinear CG [28]. For these three solvers, the average iteration count per step
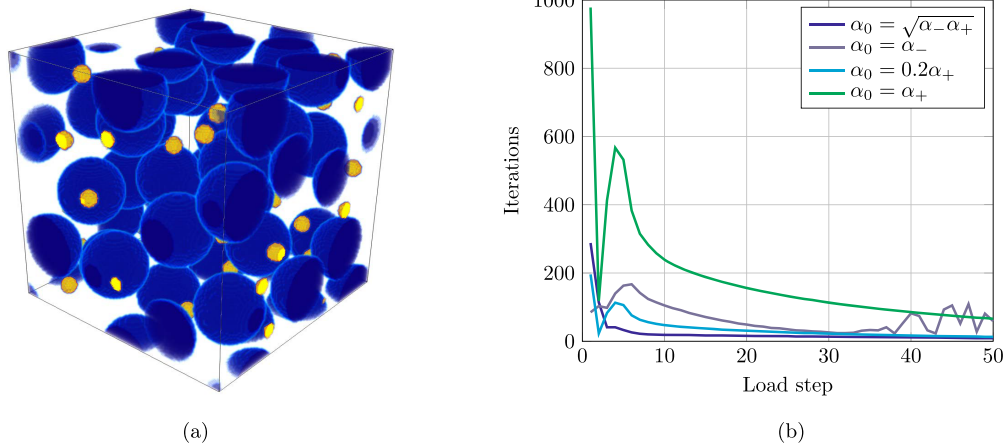

(a)

(b)

FIGURE 9 | Metal-matrix composite microstructure. (a) Geometry of the microstructure; (b) Iteration count per load step for a fixed damping factor $\gamma = 0.25$.

TABLE 4 | Mechanical properties for the metal-matrix composite [71].

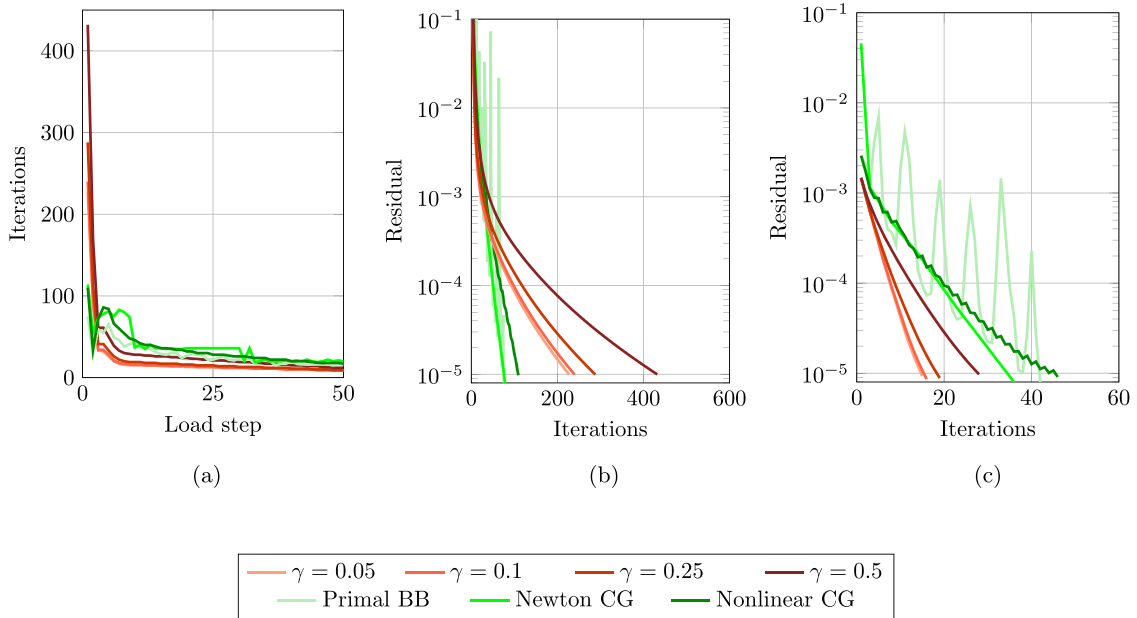| Inclusions	E = 400 GPa	v = 0.2			
Matrix	E = 75 GPa	v = 0.3	σ_Y = 75 MPa	k = 416 MPa	m = 0.3895

FIGURE 10 | Metal matrix composite: multiple load steps. (a) Iteration count per step for various solvers; (b) Convergence behaviour: First load step; (c) Convergence behaviour: Tenth load step.

ranges from 28.1 for BB to 38.0 for Newton CG. As in the previous example, the DEM schemes with a reference material $\alpha_0 = \sqrt{\alpha_+ \alpha_-}$ and damping factors $\gamma = 0.05$, $\gamma = 0.1$ and $\gamma = 0.25$ yield lower iteration counts per step, between 19.2 and 23.3, than the primal approaches. The $\gamma = 0.5$-DEM approach falls among the primal schemes in terms of iteration count, with 34.2 iterations per step on average. Investigating in more details on the convergence behavior of specific load-steps reveals that the convergence rate of DEM approach is lower than the convergence rate of primal approaches for the first step. For the tenth load step, the DEM schemes converge at a faster rate than nonlinear CG and BB. The Newton-CG scheme has a vaster convergence rate than the DEM scheme with a damping factor $\gamma = 0.5$, but converges in more iterations because of a higher initial residual. In conclusion, the example at hand confirms that polarization approaches are efficient alternatives to primal approaches for computing the nonlinear behavior of porous microstructures.

6 | Conclusions and Perspectives

In this work, we investigated the convergence of polarization methods [35, 36, 38] in the framework of FFT-based computational homogenization for porous microstructure. While it has been proved that primal approaches converge linearly for porous material [48], a linear convergence result of polarization schemes was exhibited only for linear composites and adaptive damping parameters by Sab et al. [49]. We proved the linear convergence of the damped Eyre–Milton scheme with a fixed non-trivial damping factor in a general framework including mixed stress-strain

boundary conditions and nonlinear material behavior. We exhibited sharper estimates than Sab et al. [49] on the convergence rate, and showed that any damping value in the open interval $(0, 1)$ leads to linear convergence. Such theoretical findings were supported by numerical experiments on complex microstructures. Granted that a stable discretization scheme such as the staggered grid [7] was used, all numerical experiments exhibited linear convergence.

The convergence analysis showed that the theoretical bound is optimal of a damping factor $\gamma = 0.5$, that is, for the Michel–Moulinec–Suquet [36] scheme. For such a damping factor, the reference material that optimizes the bound is always in the interval $(0, \sqrt{\alpha_+ \alpha_-}]$. The numerical experiments confirmed that the reference material maximizing the convergence rate is contained in this interval. However, the numerical experiments also revealed that the theoretical bound may not be optimal. Indeed, the damping factors that minimized the convergence rate lay between $\gamma = 0.05$ and $\gamma = 0.1$ consistently. Interestingly, these values are similar to the optimal damping factors obtained by Sab et al. [49] in the elastic case.

The experiments also showed that using a well-chosen constant damping factor decreases the number of iterations to convergence by 55 to 90% compared to using the value $\gamma = 0.5$ stemming from the convergence analysis. By comparison, choosing the reference material $\alpha_0 = \sqrt{\alpha_+ \alpha_-}$ if it is not optimal increased the number of iterations by a factor up to 17. Even though a wise choice of the damping factor accelerates convergence, it is not able to repair a bad choice of reference material. Hence, it appears that the choice

of the reference material is more important than the considered damping factor. However, to reach optimal performance, both the reference material and the damping factor need to be tuned.

A comparison to primal solvers in the elastic framework showed that the damped Eyre–Milton scheme with optimized damping and reference material could be as fast as the conjugate gradient scheme [27], and faster than the primal Barzilai-Borwein scheme [22]. However, determining the optimal DEM parameters is tedious, and polarization-based schemes with adaptive reference material and fixed damping factor are still less efficient than primal solvers. When it comes to nonlinear behavior, the results of the two examples investigated indicate that the DEM scheme outperforms primal approaches for a wise choice of reference material and a damping factor comprised between $\gamma = 0.05$ and $\gamma = 0.25$. In with such parameters, polarization schemes lower the iteration count by a factor of up to two, at least for the examples considered.

Future work may be devoted to improving the theoretical bound to get more refined estimates of the value of the optimal damping factor and reference material. An extension of the proposed analysis to the case of rigid inclusions, as proposed by Sab et al. [49], can also be envisaged.

Data Availability Statement

The data that support the findings of this study are available from the corresponding author upon reasonable request.

References

1. H. Moulinec and P. Suquet, "A Fast Numerical Method for Computing the Linear and Nonlinear Mechanical Properties of Composites," *Comptes Rendus de l'Académie des Sciences. Série II* 318, no. 11 (1994): 1417–1423.

2. H. Moulinec and P. Suquet, "A Numerical Method for Computing the Overall Response of Nonlinear Composites With Complex Microstructure," *Computer Methods in Applied Mechanics and Engineering* 157 (1998): 69–94.

3. R. Lebensohn and A. Rollett, "Spectral Methods for Full-Field Micromechanical Modelling of Polycrystalline Materials," *Computational Materials Science* 173 (2020): 109336.

4. S. Lucarini, M. V. Upadhyay, and J. Segurado, "FFT Based Approaches in Micromechanics: Fundamentals, Methods and Applications," *Modelling and Simulation in Materials Science and Engineering* 30, no. 2 (2021): 023002.

5. M. Schneider, "A Review of Non-Linear FFT-Based Computational Homogenization Methods," *Acta Mechanica* 232 (2021): 2051–2100.

6. F. Willot, "Fourier-Based Schemes for Computing the Mechanical Response of Composites With Accurate Local Fields," *Comptes Rendus Mécanique* 343 (2015): 232–245.

7. M. Schneider, F. Ospald, and M. Kabel, "Computational Homogenization of Elasticity on a Staggered Grid," *International Journal for Numerical Methods in Engineering* 105, no. 9 (2016): 693–720.

8. M. Schneider, D. Merkert, and M. Kabel, "FFT-Based Homogenization for Microstructures Discretized by Linear Hexahedral Elements," *International Journal for Numerical Methods in Engineering* 109 (2017): 1461–1489.

9. M. Leuschner and F. Fritzen, "Fourier-Accelerated Nodal Solvers (FANS) for homogenization problems," *Computational Mechanics* 62 (2018): 359–392.

10. A. Wiegmann and A. Zemitis, "EJ-HEAT: A Fast Explicit Jump Harmonic Averaging Solver for the Effective Heat Conductivity of Composite Materials," *Berichte des Fraunhofer ITWM* 94 (2006): 1–21.

11. C. Dorn and M. Schneider, "Lippmann-Schwinger Solvers for the Explicit Jump Discretization for Thermal Computational Homogenization Problems," *International Journal for Numerical Methods in Engineering* 118, no. 11 (2019): 631–653.

12. G. Bonnet, "Effective Properties of Elastic Periodic Composite Media With Fibers," *Journal of the Mechanics and Physics of Solids* 55 (2007): 881–899.

13. J. Vondřejc, "Improved Guaranteed Computable Bounds on Homogenized Properties of Periodic Media By the Fourier-Galerkin Method With Exact Integration," *International Journal for Numerical Methods in Engineering* 107 (2016): 1106–1135.

14. V. Monchiet, "Combining FFT methods and Standard Variational Principles to Compute Bounds and Estimates for the Properties of Elastic Composites," *Computer Methods in Applied Mechanics and Engineering* 283 (2015): 454–473.

15. S. Brisard and L. Dormieux, "FFT-Based Methods for the Mechanics of Composites: a General Variational Framework," *Computational Materials Science* 49, no. 3 (2010): 663–671.

16. S. Brisard and L. Dormieux, "Combining Galerkin Approximation Techniques With the Principle of Hashin And Shtrikman to Derive a New FFT-Based Numerical Method for the Homogenization of Composites," *Computer Methods in Applied Mechanics and Engineering* 217 – 220 (2012): 197–212.

17. F. Tu, Y. Jiao, X. Zhou, Y. Cheng, and F. Tan, "The Implementation of B-Splines to Hashin and Shtrikman Variational Principle Based FFT Method for the Homogenization of Composite," *International Journal of Solids and Structures* 191–192 (2020): 133–145.

18. T. Kaiser, T. Raasch, J. J. C. Remmers, and M. G. D. Geers, "A Wavelet-Enhanced Adaptive Hierarchical FFT-Based Approach For the Efficient Solution of Microscale Boundary Value Problems," *Computer Methods in Applied Mechanics and Engineering* 409 (2023): 115959.

19. L. Jabs and M. Schneider, "A Consistent Discretization via the Finite Radon Transform For FFT-Based Computational Micromechanics," *Computational Mechanics* (2024): 1–20.

20. M. Kabel, T. Böhlke, and M. Schneider, "Efficient Fixed Point and Newton-Krylov Solvers for FFT-Based Homogenization of Elasticity at Large Deformations," *Computational Mechanics* 54, no. 6 (2014): 1497–1514.

21. J. Barzilai and J. M. Borwein, "Two-Point Step Size Gradient Methods," *IMA Journal of Numerical Analysis* 8 (1988): 141–148.

22. M. Schneider, "On the Barzilai-Borwein Basic Scheme in FFT-Based Computational Homogenization," *International Journal for Numerical Methods in Engineering* 118, no. 8 (2019): 482–494.

23. M. Schneider, "An FFT-Based Fast Gradient Method for Elastic and Inelastic Unit Cell Homogenization Problems," *Computer Methods in Applied Mechanics and Engineering* 315 (2017): 846–866.

24. F. Ernesti, M. Schneider, and T. Böhlke, "Fast Implicit Solvers for Phase Field Fracture Problems on Heterogeneous Microstructures," *Computer Methods in Applied Mechanics and Engineering* 363 (2020): 112793.

25. Y. Chen, L. Gélébart, C. Chateau, M. Bornert, C. Sauder, and A. King, "Analysis of the Damage Initiation in a SiC/SiC Composite Tube From a Direct Comparison Between Large-Scale Numerical Simulation and Synchrotron X-Ray Micro-Computed Tomography," *International Journal of Solids and Structures* 161 (2019): 111–126.

26. D. Wicht, M. Schneider, and T. Böhlke, "Anderson-Accelerated Polarization Schemes for FFT-Based Computational Homogenization," *International Journal for Numerical Methods in Engineering* 122, no. 9 (2021): 2287–2311.

27. J. Zeman, J. Vondřejc, J. Novák, and I. Marek, "Accelerating a FFT-Based Solver for Numerical Homogenization of Periodic Media by Conjugate Gradients," *Journal of Computational Physics* 229, no. 21 (2010): 8065–8071.

28. M. Schneider, "A Dynamical View of Nonlinear Conjugate Gradient Methods With Applications To FFT-Based Computational Micromechanics," *Computational Mechanics* 66 (2020): 239–257.

29. N. Lahellec, J. C. Michel, H. Moulinec, and P. Suquet, "Analysis of Inhomogeneous Materials at Large Strains Using Fast Fourier Transforms," in *IUTAM Symposium on Computational Mechanics of Solid Materials at Large Strains* (Netherlands: Springer, 2003), 247–258.

30. L. Gélébart and R. Mondon-Cancel, "Non-Linear Extension of FFT-Based Methods Accelerated by Conjugate Gradients to Evaluate the Mechanical Behavior of Composite Materials," *Computational Materials Science* 77 (2013): 430–439.

31. D. Wicht, M. Schneider, and T. Böhlke, "On Quasi-Newton Methods in FFT-Based Micromechanics," *International Journal for Numerical Methods in Engineering* 121, no. 8 (2020): 1665–1694.

32. G. W. Milton, *The Theory of Composites* (Cambridge: Cambridge University Press, 2002).

33. K. Bhattacharya and P. Suquet, "A Model Problem Concerning Recoverable Strains Of Shape-memory Polycrystals," *Proceedings of the Royal Society A* 461 (2005): 2797–2816.

34. D. Wicht, M. Schneider, and T. Böhlke, "An Efficient Solution Scheme for Small-Strain Crystal-Elasto-Viscoplasticity in a Dual Framework," *Computer Methods in Applied Mechanics and Engineering* 358 (2020): 112611.

35. D. J. Eyre and G. W. Milton, "A Fast Numerical Scheme for Computing the Response of Composites Using Grid Refinement," *European Physical Journal Applied Physics* 6, no. 1 (1999): 41–47.

36. J. C. Michel, H. Moulinec, and P. Suquet, "A Computational Method Based on Augmented Lagrangians and Fast Fourier Transforms for Composites With High Contrast," *Computer Modelling in Engineering and Sciences* 1, no. 2 (2000): 79–88.

37. J. C. Michel, H. Moulinec, and P. Suquet, "A Computational Scheme for Linear and Non-Linear Composites With Arbitrary Phase Contrast," *International Journal for Numerical Methods in Engineering* 52 (2001): 139–160.

38. V. Monchiet and G. Bonnet, "A Polarization-Based FFT Iterative Scheme for Computing the Effective Properties of Elastic Composites With Arbitrary Contrast," *International Journal for Numerical Methods in Engineering* 89 (2012): 1419–1436.

39. V. Monchiet and G. Bonnet, "Numerical Homogenization of Nonlinear Composites With A Polarization-Based FFT Iterative Scheme," *Computational Materials Science* 79 (2013): 276–283.

40. H. Moulinec and F. Silva, "Comparison of Three Accelerated FFT-Based Schemes For Computing the Mechanical Response of Composite Materials," *International Journal for Numerical Methods in Engineering* 97 (2014): 960–985.

41. M. Schneider, D. Wicht, and T. Böhlke, "On Polarization-Based Schemes for the FFT-Based Computational Homogenization of Inelastic Materials," *Computational Mechanics* 64, no. 4 (2019): 1073–1095.

42. D. W. Peaceman and H. H. Rachford, "The Numerical Solution of Parabolic and Elliptic Differential Equations," *Journal of the Society for Industrial and Applied Mathematics* 3, no. 1 (1955): 28–41.

43. J. Douglas and H. H. Rachford, "On the Numerical Solution of Heat Conduction Problems in Two and Three Space Variables," *Transactions of the American Mathematical Society* 82 (1956): 421–439.

44. P. Giselsson and S. Boyd, "Linear Convergence and Metric Selection for Douglas-Rachford splitting and ADMM," *IEEE Transactions on Automatic Control* 62 (2017): 532–544.

45. H. Zhou and K. Bhattacharya, "Accelerated Computational Micromechanics and its Application to Polydomain Liquid Crystal Elastomers," *Journal of the Mechanics and Physics of Solids* 153 (2022): 104470.

46. M. Schneider, "On Non-Stationary Polarization Methods in FFT-Based Computational Micromechanics," *International Journal for Numerical Methods in Engineering* 122, no. 22 (2021): 6800–6821.

47. H. Moulinec, P. Suquet, and G. W. Milton, "Convergence of Iterative Methods Based on Neumann Series for Composite Materials: Theory and Practice," *International Journal for Numerical Methods in Engineering* 114, no. 10 (2018): 1103–1130.

48. M. Schneider, "Lippmann-Schwinger Solvers for the Computational Homogenization of Materials With Pores," *International Journal for Numerical Methods in Engineering* 121, no. 22 (2020): 5017–5041.

49. K. Sab, J. Bleyer, S. Brisard, and M. Dolbeau, "An FFT-Based Adaptive Polarization Method for Infinitely Contrasted Media With Guaranteed Convergence," *Computer Methods in Applied Mechanics and Engineering* 427 (2024): 117012.

50. H. H. Bauschke and P. L. Combettes, *Convex Analysis And Monotone Operator Theory in Hilbert Spaces* (Springer: CMS Books in Mathematics, 2011).

51. E. K. Ryu and W. Yin, *Large-Scale Convex Optimization - Algorithms & Analyses via Monotone Operators* (Cambridge: Cambridge University Press, 2022).

52. M. Ladecký, R. J. Leute, A. Falsafilig, et al., "An Optimal Preconditioned FFT-Accelerated Filig;Nite Element Solver for Homogenization," *Applied Mathematics and Computation* 446 (2023): 127835.

53. A. Finel, "A Fast and Robust Discrete FFT-based Solver for Computational Homogenization," *arXiv* 2405, no. 11168 (2024): 1–34.

54. H. Rademacher, "Über partielle und totale Differenzierbarkeit von Funktionen mehrerer Variabeln und über die Transformation der Doppelintegrale," *Mathematische Annalen* 79, no. 4 (1919): 340–359.

55. M. Kabel, S. Fliegener, and M. Schneider, "Mixed Boundary Conditions for FFT-Based Homogenization at Finite Strains," *Computational Mechanics* 57, no. 2 (2016): 193–210.

56. C. Miehe, "Strain-Driven Homogenization of Inelastic Microstructures and Composites Based on an Incremental Variational Formulation," *International Journal for Numerical Methods in Engineering* 55 (2002): 1285–1322.

57. M. Ortiz and L. Stainier, "The Variational Formulation of Viscoplastic Constitutive Updates," *Computer Methods in Applied Mechanics and Engineering* 171, no. 3–4 (1999): 419–444.

58. P. Giselsson, "Tight Global Linear Convergence Rate Bounds for Douglas–Rachford Splitting," *Fixed Point Theory and Applications* 19 (2017): 2241–2270.

59. M. Schneider, "Voxel-Based Finite Elements With Hourglass Control in FFT-Based Computational Homogenization," *International Journal for Numerical Methods in Engineering* 123, no. 24 (2022): 6286–6313.

60. M. Frigo and S. G. Johnson, "The Design and Implementation of FFTW3," *Proceedings of the IEEE* 93 (2005): 216–231.

61. S. Williams and A. Philipse, "Random Packings of Spheres and Spherocylinders Simulated by Mechanical Contraction," *Physical Review E* 67 (2003): 1–9.

62. M. Schneider, T. Hofmann, H. Andrä, et al., "Modeling the Microstructure and Computing Effective Elastic Properties of Sand Core

Materials," *International Journal of Solids and Structures* 143 (2018): 1–17.

63. T. Wichtmann and T. Triantafyllidis, "On the Influence of the Grain Size Distribution Curve on P-Wave Velocity, Constrained Elastic Modulus M_{max} and Poisson's Ratio of Quartz Sands," *Soil Dynamics and Earthquake Engineering* 30, no. 8 (2010): 757–766.

64. N. P. Daphalapurkar, F. Wang, B. Bu, H. Lu, and R. Komanduri, "Determination of Mechanical Properties of Sand Grains by Nanoindentation," *Experimental Mechanics* 51 (2011): 719–728.

65. D. S. Sanditov, V. V. Mantatov, and B. D. Sanditov, "Poisson Ratio and Plasticity of Glasses," *Technical Physics* 54, no. 4 (2009): 594–596.

66. Z. Xu, M. A. T. Figueiredo, X. Yuan, C. Studer, and T. Goldstein, "Adaptive Relaxed ADMM: Convergence Theory and Practical Implementation," *in IEEE Conference on Computer Vision and Pattern Recognition* (CVPR) (2017): 7234–7243.

67. Z. Xu, M. A. T. Figueiredo, and T. Goldstein, "Adaptive ADMM with Spectral Penalty Parameter Selection," *in Proceedings of the 20th International Conference on Artificial Intelligence and Statistics* (2017): 718–727.

68. B. S. He, H. Yang, and S. L. Wang, "Alternating Direction Method with Self-Adaptive Penalty Parameters for Monotone Variational Inequalities," *Journal of Optimization Theory and Applications* 106, no. 2 (2000): 337–356.

69. D. A. Lorenz and Q. Tran-Dinh, "Non-Stationary Douglas–Rachford and Alternating Direction Method of Multipliers: Adaptive Step-Sizes and Convergence," *Computational Optimization and Applications* 74 (2019): 67–92.

70. C. Lautensack, "Fitting Three-Dimensional Laguerre Tessellations to Foam Structures," *Journal of Applied Statistics* 35, no. 9 (2008): 985–995.

71. J. Segurado, J. Llorca, and C. González, "On the Accuracy of Mean-Field Approaches to Simulate the Plastic Deformation of Composites," *Scripta Materialia* 46, no. 7 (2002): 525–529.

72. M. Schneider, "The Sequential Addition and Migration Method to Generate Representative Volume Elements for the Homogenization of Short Fiber Reinforced Plastics," *Computational Mechanics* 59 (2017): 247–263.

73. A. Mehta and M. Schneider, "A Sequential Addition and Migration Method for Generating Microstructures of Short Fibers With Prescribed Length Distribution," *Computational Mechanics* 70, no. 4 (2022): 829–851.

74. I. Doghri, L. Brassart, L. Adam, and J.-S. Gérard, "A Second-Moment Incremental Formulation for the Mean-Field Homogenization of Elasto-Plastic Composites," *International Journal of Plasticity* 27, no. 3 (2011): 352–371.

75. K. O. Friedrichs, "On the Boundary Value Problems of the Theory Of Elasticity and Korn's Inequality," *Annals of Mathematics* 48 (1947): 441–471.

Appendix A

Out-Sourced Mathematical Derivations

A1 | The Formula for the Residual

The goal of this appendix is to establish the validity of the representation formula (85)

$$R(P) = 2\,\mathbb{C}^0 : \tilde{\Gamma}^c : (\varepsilon - \overline{\varepsilon}) + 2\,\tilde{\Gamma} : (\sigma - \overline{\sigma}) \qquad (A1)$$

for the residual (84). Our starting points are the definitions (76) and (84), that is, we have the identity

$$R(P) = P - \mathbb{Y} : Z^0(P) - 2\,\mathbb{C}^0 : \overline{\varepsilon} - 2\,\overline{\sigma} \qquad (A2)$$

Combining the Equations (59) and (67) in the form

$$P = \sigma + \mathbb{C}^0 : \varepsilon \quad \text{and} \quad Z^0(P) = \sigma - \mathbb{C}^0 : \varepsilon \qquad (A3)$$

for the fields (87) and the representation formula implied by the definitions (60) and (86)

$$\mathbb{Y} = \mathrm{Id} - 2\,\tilde{\Gamma} \qquad (A4)$$

we observe

$$
\begin{aligned}
P - \mathbb{Y} : Z^0(P) &= \sigma + \mathbb{C}^0 : \varepsilon - (\mathrm{Id} - 2\,\tilde{\Gamma}) : (\sigma - \mathbb{C}^0 : \varepsilon) \\
&= \sigma + \mathbb{C}^0 : \varepsilon - \sigma + \mathbb{C}^0 : \varepsilon + 2\,\tilde{\Gamma} : (\sigma - \mathbb{C}^0 : \varepsilon) \quad (A5)\\
&= 2\,\mathbb{C}^0 : \varepsilon - 2\,\mathbb{C}^0 : \tilde{\Gamma} : \varepsilon + 2\,\tilde{\Gamma} : \sigma
\end{aligned}
$$

As we work with a diagonal reference material $\mathbb{C}^0 = \alpha_0\,\mathrm{Id}$ and by definition (86) of the operator $\tilde{\Gamma}^c$, we may rewrite Equation (A5) in the form

$$P - \mathbb{Y} : Z^0(P) = 2\,\mathbb{C}^0 : \tilde{\Gamma}^c : \varepsilon + 2\,\tilde{\Gamma} : \sigma \qquad (A6)$$

As the operator Γ defined in Equation (60) annihilates homogeneous fields, we have the identities

$$\tilde{\Gamma} : \overline{\sigma} = \overline{\sigma} \quad \text{and} \quad \tilde{\Gamma}^c : \overline{\varepsilon} = \overline{\varepsilon} \qquad (A7)$$

where we used the compatibility conditions (57). Combining this insight with Equation (A2) and the representation (A6) yields the claim (A1).

A2 | The Lower Bound for the Residual

In this paragraph, we would like to establish the validity of the estimate (92)

$$
\begin{aligned}
\frac{1}{2}&\left(R(P_1) - R(P_2),\, P_1 - P_2\right)_{L^2} \\
&\geq \frac{\alpha_0}{\alpha_+ + \alpha_0}\,\frac{1}{|Y|}\int_Y \left\|\tilde{\Gamma}^c : (P_1 - P_2)\right\|^2 d\boldsymbol{x} \\
&\quad + \frac{\alpha_-}{\alpha_- + \alpha_0}\,\frac{1}{|Y|}\int_{Y \setminus Y_p} \left\|\tilde{\Gamma} : (P_1 - P_2)\right\|^2 d\boldsymbol{x}
\end{aligned}
\qquad (A8)
$$

We will assume that the free energy (47)-and thus also the operators J^0 and K^0 are smooth in the second variable. Then, we will infer the fundamental Theorem of calculus to transfer the linear elastic arguments of Sab et al. [49] to the setting at hand. At the end of this section, we will briefly discuss how the case of general free energy (47) is followed by a mollification argument.

By the representation formula (85) for the residual and accounting for the definition (87)

$$R(P) = 2\,\tilde{\Gamma}^c : (J^0(P) - \mathbb{C}^0 : \overline{\varepsilon}) + 2\,\tilde{\Gamma} : (K^0(P) - \overline{\sigma}) \qquad (A9)$$

we arrive at the formula

$$
\begin{aligned}
R(P_1) &- R(P_2) \\
&= 2\,\tilde{\Gamma}^c : (K^0(P_1) - K^0(P_2)) + 2\,\tilde{\Gamma} : (J^0(P_1) - J^0(P_2))
\end{aligned}
\qquad (A10)
$$

As we assumed smoothness in the tensor variable, we may use the fundamental Theorem of calculus to write

$$
\begin{aligned}
J^0(P_1)(\boldsymbol{x}) - J^0(P_2)(\boldsymbol{x}) = \int_0^1 \mathbb{J}^0(\boldsymbol{x}, P_2(\boldsymbol{x}) + s(P_1(\boldsymbol{x}) - P_2(\boldsymbol{x}))) : \\
(P_1(\boldsymbol{x}) - P_2(\boldsymbol{x}))\, ds
\end{aligned}
\qquad (A11)
$$

and

$$
\begin{aligned}
K^0(P_1)(\boldsymbol{x}) - K^0(P_2)(\boldsymbol{x}) = \int_0^1 \mathbb{K}^0(\boldsymbol{x}, P_2(\boldsymbol{x}) + s(P_1(\boldsymbol{x}) - P_2(\boldsymbol{x}))) : \\
(P_1(\boldsymbol{x}) - P_2(\boldsymbol{x}))\, ds
\end{aligned}
$$
$$(A12)$$

where the tensor fields $\mathbb{J}^0$ and $\mathbb{K}^0$ correspond to the derivatives of the operators $\boldsymbol{J}^0$ and $\boldsymbol{K}^0$ in the tensor variable. Thus, the formula (A10) becomes

$$\boldsymbol{R}(\boldsymbol{P}_1) - \boldsymbol{R}(\boldsymbol{P}_2) = 2 \int_0^1 \left(\tilde{\boldsymbol{\Gamma}} : \mathbb{J}^0 + \tilde{\boldsymbol{\Gamma}}^c : \mathbb{K}^0 \right) : (\boldsymbol{P}_1 - \boldsymbol{P}_2) \, ds \quad \text{(A13)}$$

where we suppress the arguments of the fields $\mathbb{J}^0$ and $\mathbb{K}^0$ for notational convenience. Taking the L^2-inner product with the field $\boldsymbol{P}_1 - \boldsymbol{P}_2$ leads to the expression

$$\begin{aligned}
\frac{1}{2} &\left(\boldsymbol{R}(\boldsymbol{P}_1) - \boldsymbol{R}(\boldsymbol{P}_2), \boldsymbol{P}_1 - \boldsymbol{P}_2 \right)_{L^2} \\
&= \int_0^1 \left(\tilde{\boldsymbol{\Gamma}} : \mathbb{J}^0 : (\boldsymbol{P}_1 - \boldsymbol{P}_2), \boldsymbol{P}_1 - \boldsymbol{P}_2 \right)_{L^2} \\
&\quad + \left(\tilde{\boldsymbol{\Gamma}}^c : \mathbb{K}^0 : (\boldsymbol{P}_1 - \boldsymbol{P}_2), \boldsymbol{P}_1 - \boldsymbol{P}_2 \right)_{L^2} ds \\
&= \int_0^1 \left(\mathbb{J}^0 : (\boldsymbol{P}_1 - \boldsymbol{P}_2), \tilde{\boldsymbol{\Gamma}} : (\boldsymbol{P}_1 - \boldsymbol{P}_2) \right)_{L^2} \\
&\quad + \left(\mathbb{K}^0 : (\boldsymbol{P}_1 - \boldsymbol{P}_2), \tilde{\boldsymbol{\Gamma}}^c : (\boldsymbol{P}_1 - \boldsymbol{P}_2) \right)_{L^2} ds
\end{aligned} \quad \text{(A14)}$$

where we used that the operators (86) are orthogonal, in particular self-adjoint. The complementarity of the orthogonal projectors (86) permits us to decompose

$$\boldsymbol{P}_1 - \boldsymbol{P}_2 = \tilde{\boldsymbol{\Gamma}} : (\boldsymbol{P}_1 - \boldsymbol{P}_2) + \tilde{\boldsymbol{\Gamma}}^c : (\boldsymbol{P}_1 - \boldsymbol{P}_2) \quad \text{(A15)}$$

so that we are led to the (lengthy) expression

$$\begin{aligned}
\frac{1}{2} &\left(\boldsymbol{R}(\boldsymbol{P}_1) - \boldsymbol{R}(\boldsymbol{P}_2), \boldsymbol{P}_1 - \boldsymbol{P}_2 \right)_{L^2} \\
&= \int_0^1 \left(\mathbb{J}^0 : \tilde{\boldsymbol{\Gamma}} : (\boldsymbol{P}_1 - \boldsymbol{P}_2), \tilde{\boldsymbol{\Gamma}} : (\boldsymbol{P}_1 - \boldsymbol{P}_2) \right)_{L^2} \\
&\quad + \left(\mathbb{J}^0 : \tilde{\boldsymbol{\Gamma}}^c : (\boldsymbol{P}_1 - \boldsymbol{P}_2), \tilde{\boldsymbol{\Gamma}} : (\boldsymbol{P}_1 - \boldsymbol{P}_2) \right)_{L^2} ds \\
&\quad + \left(\mathbb{K}^0 : \tilde{\boldsymbol{\Gamma}} : (\boldsymbol{P}_1 - \boldsymbol{P}_2), \tilde{\boldsymbol{\Gamma}}^c : (\boldsymbol{P}_1 - \boldsymbol{P}_2) \right)_{L^2} ds \\
&\quad + \left(\mathbb{K}^0 : \tilde{\boldsymbol{\Gamma}}^c : (\boldsymbol{P}_1 - \boldsymbol{P}_2), \tilde{\boldsymbol{\Gamma}}^c : (\boldsymbol{P}_1 - \boldsymbol{P}_2) \right)_{L^2} ds
\end{aligned} \quad \text{(A16)}$$

The operators $\mathbb{J}^0$ and $\mathbb{K}^0$ are self-adjoint, that is, satisfy the major symmetry, and obey the identity

$$\mathbb{J}^0 + \mathbb{K}^0 = \text{Id} \quad \text{(A17)}$$

The latter (linear) identity is a consequence of differentiating the (nonlinear) identity (62). The fact that $\mathbb{J}^0$ and $\mathbb{K}^0$ are self-adjoint follows from the fact that both are Hessians of certain functions, that is, those whose gradient corresponds to the resolvent and reflected resolvent, respectively. More precisely, Lagrangian duality is involved with that.

Thus, for any $\boldsymbol{Q} \in L^2(Y; \text{Sym}(d))$ it holds that

$$\begin{aligned}
&\left(\mathbb{J}^0 : \tilde{\boldsymbol{\Gamma}}^c : \boldsymbol{Q}, \tilde{\boldsymbol{\Gamma}} : \boldsymbol{Q} \right)_{L^2} + \left(\mathbb{K}^0 : \tilde{\boldsymbol{\Gamma}} : \boldsymbol{Q}, \tilde{\boldsymbol{\Gamma}}^c : \boldsymbol{Q} \right)_{L^2} \\
&= \left(\mathbb{J}^0 : \tilde{\boldsymbol{\Gamma}}^c : \boldsymbol{Q}, \tilde{\boldsymbol{\Gamma}} : \boldsymbol{Q} \right)_{L^2} + \left(\tilde{\boldsymbol{\Gamma}} : \boldsymbol{Q}, \mathbb{K}^0 : \tilde{\boldsymbol{\Gamma}}^c : \boldsymbol{Q} \right)_{L^2} \\
&= \left(\left[\mathbb{J}^0 + \mathbb{K}^0 \right] : \tilde{\boldsymbol{\Gamma}}^c : \boldsymbol{Q}, \tilde{\boldsymbol{\Gamma}} : \boldsymbol{Q} \right)_{L^2} \\
&= \left(\tilde{\boldsymbol{\Gamma}}^c : \boldsymbol{Q}, \tilde{\boldsymbol{\Gamma}} : \boldsymbol{Q} \right)_{L^2} \\
&= 0
\end{aligned} \quad \text{(A18)}$$

where we used the fact that the orthogonal projectors $\tilde{\boldsymbol{\Gamma}}$ and $\tilde{\boldsymbol{\Gamma}}^c$ are complementary. Applying the last insight (A18) to the case $\boldsymbol{Q} = \boldsymbol{P}_1 - \boldsymbol{P}_2$ and integrating, permits to rewrite Equation (A16) in the form

$$\begin{aligned}
\frac{1}{2} &\left(\boldsymbol{R}(\boldsymbol{P}_1) - \boldsymbol{R}(\boldsymbol{P}_2), \boldsymbol{P}_1 - \boldsymbol{P}_2 \right)_{L^2} \\
&= \int_0^1 \left(\mathbb{J}^0 : \tilde{\boldsymbol{\Gamma}} : (\boldsymbol{P}_1 - \boldsymbol{P}_2), \tilde{\boldsymbol{\Gamma}} : (\boldsymbol{P}_1 - \boldsymbol{P}_2) \right)_{L^2} \\
&\quad + \left(\mathbb{K}^0 : \tilde{\boldsymbol{\Gamma}}^c : (\boldsymbol{P}_1 - \boldsymbol{P}_2), \tilde{\boldsymbol{\Gamma}}^c : (\boldsymbol{P}_1 - \boldsymbol{P}_2) \right)_{L^2} ds
\end{aligned} \quad \text{(A19)}$$

The linearization of a nonlinear strongly monotone operator is also strongly monotone with the same strong monotonicity constant. As the operators $\mathbb{J}^0$ and $\mathbb{K}^0$ linearize the strongly monotone operators $\boldsymbol{J}^0$ and $\boldsymbol{K}^0$, the estimates (69) and (70) imply the lower bounds

$$\left(\mathbb{J}^0(\boldsymbol{x}, \boldsymbol{T}) : \tilde{\boldsymbol{\Gamma}} : \boldsymbol{Q}, \tilde{\boldsymbol{\Gamma}} : \boldsymbol{Q} \right)_{L^2} \geq \frac{\alpha_-}{\alpha_- + \alpha_0} \| \tilde{\boldsymbol{\Gamma}} : \boldsymbol{Q} \|^2 \quad \text{(A20)}$$

and

$$\left(\mathbb{K}^0(\boldsymbol{x}, \boldsymbol{T}) : \tilde{\boldsymbol{\Gamma}}^c : \boldsymbol{Q}, \tilde{\boldsymbol{\Gamma}}^c : \boldsymbol{Q} \right)_{L^2} \geq \frac{\alpha_0}{\alpha_+ + \alpha_0} \| \tilde{\boldsymbol{\Gamma}}^c : \boldsymbol{Q} \|^2 \quad \text{(A21)}$$

in the skeleton $Y \setminus Y_p \ni \boldsymbol{x}$ and for arbitrary $\boldsymbol{T}, \boldsymbol{Q} \in \text{Sym}(d)$. In the pore space, the identities

$$\mathbb{J}^0(\boldsymbol{x}, \boldsymbol{T}) = \boldsymbol{0} \quad \text{and} \quad \mathbb{K}^0(\boldsymbol{x}, \boldsymbol{T}) = \text{Id}, \quad \boldsymbol{x} \in Y_p, \quad \boldsymbol{T} \in \text{Sym}(d) \quad \text{(A22)}$$

hold. Thus, the desired estimate (A8) follows.

Last but not least let us briefly comment on the assumed smoothness of the free energy in the tensor variable. In fact, one may use a mollifier to smooth the free energy, preserving the α_--strong monotonicity and the α_+-Lipschitz continuity of the associated stress operator in the skeleton. Then, the estimate (A8) established for the smooth case applies. The estimate (A8) for the non-smooth case then follows by letting the mollifier approach a Dirac distribution.

A3 | The Recovery Estimate in the Pore Space

The goal of this section is to show the existence of a positive constant δ, s.t. the estimate (94)

$$\int_{Y \setminus Y_p} \left\| \overline{\boldsymbol{T}} + \nabla^s \boldsymbol{u} \right\|^2 d\boldsymbol{x} \geq \delta \int_Y \left\| \overline{\boldsymbol{T}} + \nabla^s \boldsymbol{u} \right\|^2 d\boldsymbol{x} \quad \text{(A23)}$$

holds for a homogeneous strain field $\overline{\boldsymbol{T}}$ and any displacement fluctuation field $\boldsymbol{u} \in H^1_{\text{per}}(Y)^d$ which satisfies the PDE (93)

$$\text{div} \, \nabla^s \boldsymbol{u} = \boldsymbol{0} \quad \text{in the pore space} \quad Y_p \quad \text{(A24)}$$

First notice that in case the estimate (A23) holds, the constant δ cannot exceed unity. Indeed, by choosing $\overline{\boldsymbol{T}} = \boldsymbol{0}$ and a displacement field fully supported in the skeleton $Y \setminus Y_p$, a constant δ greater than unity would lead to a contradiction.

The estimate (A23) itself follows from two other bounds. For a start, there is a constant C_1, s.t. the following variant of Korn's inequality [75]

$$\int_{Y \setminus Y_p} \| \overline{\boldsymbol{T}} \|^2 + \| \nabla \boldsymbol{u} \|^2 d\boldsymbol{x} \leq C_1 \int_{Y \setminus Y_p} \left\| \overline{\boldsymbol{T}} + \nabla^s \boldsymbol{u} \right\|^2 d\boldsymbol{x} \quad \text{(A25)}$$

holds for all $\overline{\boldsymbol{T}} \in \text{Sym}(d)$ and any field $\boldsymbol{u} \in H^1_{\text{per}}(Y)^d$ which satisfies the PDE (A24). Secondly, there is a constant C_2, s.t. the estimate

$$\int_{Y_p} \| \nabla^s \boldsymbol{u} \|^2 d\boldsymbol{x} \leq C_2 \int_{Y \setminus Y_p} \| \nabla^s \boldsymbol{u} \|^2 d\boldsymbol{x} \quad \text{(A26)}$$

holds for all fields $\boldsymbol{u} \in H^1_{\text{per}}(Y)^d$ satisfying the PDE (A24). With the estimates (A25) and (A26) at hand, the desired estimate (A23) follows directly. In fact, as the symmetrized gradient of a periodic displacement fluctuation field is L^2-orthogonal to the constants, the binomial formula implies the identity

$$\int_Y \left\| \overline{\boldsymbol{T}} + \nabla^s \boldsymbol{u} \right\|^2 d\boldsymbol{x} = \int_Y \| \overline{\boldsymbol{T}} \|^2 + \| \nabla^s \boldsymbol{u} \|^2 d\boldsymbol{x} \quad \text{(A27)}$$

The estimate (A26) implies the bound

$$\int_Y \|\nabla^s \boldsymbol{u}\|^2 \, d\boldsymbol{x} = \int_{Y_p} \|\nabla^s \boldsymbol{u}\|^2 \, d\boldsymbol{x} + \int_{Y \setminus Y_p} \|\nabla^s \boldsymbol{u}\|^2 \, d\boldsymbol{x}$$
$$\le \left(1 + C_2\right) \int_{Y \setminus Y_p} \|\nabla^s \boldsymbol{u}\|^2 \, d\boldsymbol{x} \tag{A28}$$

In particular, we obtain an estimate

$$\int_Y \left\|\overline{\boldsymbol{T}} + \nabla^s \boldsymbol{u}\right\|^2 \, d\boldsymbol{x}$$
$$\le \max\left(\frac{|Y|}{|Y \setminus Y_p|}, \left(1 + C_2\right)\right) \int_{Y \setminus Y_p} \|\overline{\boldsymbol{T}}\|^2 + \|\nabla^s \boldsymbol{u}\|^2 \, d\boldsymbol{x} \tag{A29}$$
$$\le C_1 \max\left(\frac{|Y|}{|Y \setminus Y_p|}, \left(1 + C_2\right)\right) \int_{Y \setminus Y_p} \left\|\overline{\boldsymbol{T}} + \nabla^s \boldsymbol{u}\right\|^2 \, d\boldsymbol{x}$$

where we used the point-wise inequality $\|\nabla^s \boldsymbol{u}\| \le \|\nabla \boldsymbol{u}\|$ and the Korn-type estimate (A25). In particular, the desired lower bound (A23) holds with the constant

$$\delta = \frac{1}{C_1 \max\left(|Y|/|Y \setminus Y_p|, \left(1 + C_2\right)\right)} \tag{A30}$$

Thus, it remains to discuss the validity of the estimates (A25) and (A26). For the second estimate (A26), we refer to Appendix B in Schneider [48]. The first estimate (A25) is a direct consequence of the assumption (46), and is most easily established by the traditional proof strategy for Korn's inequality on a general domain. We argue by contradiction, that is, we assume that the estimate (A25) does not hold. Then, there are sequences $(\overline{\boldsymbol{T}}_k)$ and $(\boldsymbol{u}_k)$ which satisfy the equation

$$\int_{Y \setminus Y_p} \left\|\overline{\boldsymbol{T}}_k\right\|^2 + \|\nabla \boldsymbol{u}_k\|^2 \, d\boldsymbol{x} = 1 \quad \text{for all} \quad k \tag{A31}$$

but whose sum vanishes in the limit

$$\int_{Y \setminus Y_p} \left\|\overline{\boldsymbol{T}}_k + \nabla^s \boldsymbol{u}_k\right\|^2 \, d\boldsymbol{x} \to 0 \quad \text{as} \quad k \to \infty \tag{A32}$$

Due to the uniform bound implied by Equation (A31), the sequence $(\overline{\boldsymbol{T}}_k)$ is compact, that is, we may assume–possibly up to relabeling–that the sequence converges to an element $\overline{\boldsymbol{T}} \in \mathrm{Sym}(d)$. Similarly, the Rellich-Kondrachov Theorem implies that we may find an element $\boldsymbol{u} \in H^1(Y \setminus Y_p)^d$, s.t. the sequence $(\boldsymbol{u}_k)$ converges strongly in L^2 to $\boldsymbol{u}$ and whose gradients converge L^2-weakly to $\nabla \boldsymbol{u}$. In particular, the sum $\overline{\boldsymbol{T}}_k + \nabla^s \boldsymbol{u}_k$ also converges weakly in L^2 to $\overline{\boldsymbol{T}} + \nabla^s \boldsymbol{u}$. Due to the norm convergence (A32), we must necessarily have

$$\overline{\boldsymbol{T}} + \nabla^s \boldsymbol{u} = \boldsymbol{0} \tag{A33}$$

In particular, the field $\boldsymbol{u}$ has a homogeneous symmetrized gradient on the skeleton. By the assumption (46), it follows that $\overline{\boldsymbol{T}} = \boldsymbol{0}$ and $\nabla^s \boldsymbol{u} = \boldsymbol{0}$ hold separately, which is in contradiction with the starting assumption (A31). Consequently, the estimate (A25) holds.